

## Using the Discontinuous Deformation Analysis to Model Wave Propagations in Jointed Rock Masses

Y.J. Ning<sup>1,2,3</sup>, Z.Y. Zhao<sup>3</sup>, J.P. Sun<sup>3</sup> and W.F. Yuan<sup>1,2</sup>

**Abstract:** In this paper, wave propagations in jointed rock masses are modeled by the discontinuous deformation analysis (DDA) method. The selection of the numerical control parameters in the DDA for wave propagation modeling is discussed in detail, and the effects of the joint stiffness, the seismic loading frequency, the joint strength, and the incident angle on the propagations of stress waves in a jointed rock mass are modeled and analyzed. Two nonreflecting boundary conditions including the viscous boundary condition (VBC) and the superposition boundary condition (SBC) are coupled into the DDA. The applicability of the two nonreflecting boundary conditions for simple and complex wave propagation problems is verified. A blasting-induced wave propagation problem in a jointed rock mass is analyzed, in which the applicability of two blast loading application approaches, i.e., the displacement history input (DHI) and the stress history input (SHI), are studied, and the numerical derived wave propagation results are compared with the field test records. Results show that the DDA is a promising tool for the analysis of wave propagations in jointed rock masses.

**Keywords:** Discontinuous deformation analysis, wave propagation, jointed rock mass, nonreflecting boundary, blast loading.

### 1 Introduction

Rock masses are inhomogeneous and anisotropic medium consisting of intact rock elements as well as discontinuous components, including joints, faults, bedding planes, and other weakness surfaces. The various types of such discontinuities, generally referred to as joints, break up a rock mass into a discontinuous system,

<sup>1</sup> School of Manufacturing Science and Engineering, Southwest University of Science and Technology, Mianyang 621010, China

<sup>2</sup> Key Laboratory of Testing Technology for Manufacturing Process (Ministry of Education), Southwest University of Science and Technology, Mianyang 621010, China

<sup>3</sup> School of Civil and Environmental Engineering, Nanyang Technological University, Singapore 639798, Singapore

termed as a jointed rock mass. The mechanical response of a jointed rock mass under static and/or dynamic loadings is determined by the properties of the intact rock elements and of the joints as well as by the geometry of the rock system [Cook (1992)]. It is widely recognized that due to the deformation of the joints and the reflections at the joint surfaces, a stress wave will attenuate and slow down when propagating through a jointed rock mass. In rock engineering, the damage of rock structures are generally governed by the threshold values of the stress wave amplitudes, such as the peak displacement, the peak particle velocity (PPV), or the peak particle acceleration (PPA) [Zhao, Zhao, and Cai (2006)]. In geophysics, the measurements of the seismic waves can also be used to back-analyze the internal geological structures [Wang (2001)]. It is of great importance to understand the characteristics of the propagations of stress waves in a rock mass and to realize the effects of the main influencing factors. In theoretical analysis, the effects of joints on wave propagations can be considered by simplifying a jointed rock mass as an equivalent continuous medium through the definition of the effective elastic modulus [Schoenberg and Muir (1989); Schoenberg and Sayers (1995)] or the construction of equivalent constitutive models [Liu and Katsabanis (1997); Ma, Hao, and Zhou (1998)] from the point view of the entirety; Nevertheless, such assumptions lose the discreteness of wave attenuations at individual joint and the intrinsic frequency dependent property of wave propagations through joints.

On most occasions, rock joints appear in near-parallel patterns in sets and each joint has a near-planar shape. A single joint can be described as either a displacement discontinuity when the coupling between the two half spaces is of elastic stiffness, or as a velocity discontinuity if the coupling is viscous [Pyrak-Nolte, Myer, and Cook (1990a); Cook (1992)]. A displacement discontinuity results in frequency-dependent reflection and transmission coefficients and a frequency-dependent time delay, while a velocity discontinuity results in frequency-independent coefficients and zero time delay. Real joints are expected to comprise both types of discontinuities possessing elastic as well as viscous coupling across the interfaces [Cook (1992)]. Corresponding to displacement discontinuities, the displacement discontinuity model has been widely applied in the study of the elastic property of a single rock joint [e.g. Pyrak-Nolte, Myer, and Cook (1990a); Gu, Suarez-Rivera, Nihei, and Myer (1996); Li, Ma, and Huang (2010); Ma, Li, and Zhao (2011)]. In this model, a rock joint is treated as a non-welded interface of zero thickness, which is valid when the fracture is planar, large in extent, and small in thickness as compared with the wavelength. The linear displacement discontinuity model has been extended to the nonlinear hyperbolic elastic model for the analysis of wave propagations through a nonlinear rock joint as well [Zhao and Cai (2001); Li, Ma, and Zhao (2011b)].

Wave propagations through a joint set comprising multiple parallel fractures are much more complicated due to the inter-fracture wave reflections and transmissions. Based on the displacement discontinuity model, it is often difficult to analyze the effects of a joint set on wave propagations. Pyrak-Nolte, Myer, and Cook (1990b) simplified the wave propagation problem through a joint set by ignoring the multiple reflections. This method is valid only when the joint spacing is relatively large as compared with the wave length. Alternatively, the displacement discontinuity model combining the method of characteristics can be used to account for the inter-fracture multiple reflections [Cai and Zhao (2000); Zhao, Zhao, and Cai (2006)]. Moreover, an equivalent viscoelastic medium model, in which a concept of “virtual wave source” is proposed to consider the wave reflections between joints, was adopted by Li, Ma, and Zhao (2010) for rock masses with parallel joints. This model works well when the wave length is sufficiently long as compared with the joint spacing.

In natural rock masses, two or more joint sets often exist in the same domain with intersection angles of a quite wide range; each joint may be clean or coupled with filled materials and the joint spacing may also differ a lot. In earthquakes or rock blasting, the seismic waves may propagate through the rock joints from arbitrary angles; under dynamic loadings of relatively high intensity, e.g., in the near region of a blasting source, a joint will possess an extraordinarily large deformation. All these factors increase the complexity of wave propagations in a real jointed rock mass dramatically. For such complicated scenarios, numerical methods seem more promising as compared with theoretical solutions due to the rapid development of computational techniques and computer technologies.

In continuous numerical methods such as the finite element method (FEM), the finite difference method (FDM), or the boundary element method (BEM), the number of discontinuities that can be efficiently handled is limited [e.g. Lin and Ma (2011); Tserpes and Koumpias (2012)] because these methods are developed based on continuum analysis in essence. On the contrary, discontinuous numerical methods, such as the distinct element method (DEM) [Cundall (1971)] and the discontinuous deformation analysis (DDA) [Shi (1988)], which were originally developed for modeling discontinuous material systems, are especially suitable for the analysis of the mechanical behaviors of jointed rock masses. The DEM code UDEC has been widely employed to investigate the wave propagations through rock joints or in jointed rock masses [e.g. Chen and Zhao (1998); Fan, Jiao, and Zhao (2004); Lei, Hefny, Yan, and Teng (2007); Wang, Konietzky, and Shen (2009)]. The wave propagations through a single joint, multiple parallel joints, and a rock mass with two joint sets in the UDEC have been verified. Another DEM code PFC2D has also been used to study wave propagations through a single joint [Resende, Lamas,

Lemos, and Calcada (2010)].

The DDA, as one representative discontinuum-based numerical method, has been widely used in the modeling of the mechanical behaviors of jointed rock masses under static and/or dynamic loadings. The accuracy of the DDA in dealing with block kinematics has been extensively verified by many researchers, as reviewed by MacLaughlin and Doolin (2006). The application of DDA in seismic sliding prediction has been investigated in detail by Hatzor and Feintuch (2001), Wu (2010), and Ning and Zhao (2012). Jiao, Zhang, Zhao and Liu (2007), Gu and Zhao (2009), and Bao, Hatzor, and Huang (2012) studied stress wave propagation problems in DDA block systems. Using the DDA, Mortazavi and Katsabanis (2001) and Ning et al. [Ning, Yang, An, and Ma (2011); Ning, Yang, Ma, and Chen (2011)] reproduced rock mass failures and the subsequent rock block motions under blast loadings. Kong and Liu (2002), Hatzor, Arzi, Zaslavsky, and Shapira (2004), Kamai and Hatzor (2008), and Wu, Lin, and Chen (2009) simulated earthquake-induced failures of rock-fill dams, rock slopes, rock masonry structures, and landslides. Through DDA analysis of overturned columns, Yagoda-Biran and Hatzor (2010) estimated the constraining paleo PGA values of earthquakes. The DDA has also been used to analyze earthquake fault activities in the dynamic process of earthquakes [Cai, He, and Wang (2000)].

The purpose of this paper is to extend our previous research [Gu and Zhao (2009)] on wave propagations in DDA block systems and the application of the DDA method in wave propagation modeling in jointed rock masses. In this study, the joints between blocks are assumed to be dry and of linear elastic properties. Firstly, a detailed discussion on the selection of numerical control parameters in DDA modeling of wave propagations is presented, and the effects of the joint stiffness (contact spring stiffness) between blocks, the seismic loading frequency, the joint strength, and the joint direction (stress wave incident angle) on wave propagations are explored by DDA modeling of wave propagations in jointed rock bars. To solve dynamic problems in infinite medium with finite DDA models, two nonreflecting boundaries, namely, the viscous boundary and the superposition boundary, are coupled into the DDA. The absorbing abilities of the two boundary conditions in one-dimensional wave propagation problems are investigated. Thereafter, an underground blasting-induced wave propagation problem in a jointed rock mass is modeled. Two seismic loading approaches, i.e., the displacement history input (DHI) and the stress history input (SHI), are employed and discussed. The absorbing abilities of the two nonreflecting boundaries in two-dimensional problems are further verified. The numerical derived particle velocity time histories and PPVs are compared with the corresponding filed test results. The possibility of modeling two-dimensional wave propagations in jointed rock masses by the DDA is

validated.

## 2 Wave propagation analysis in jointed rock bars

### 2.1 DDA features and modeling of wave propagations

The DDA models a discontinuous medium as an assemblage of discrete rock blocks. Each block can be deformed, translated, and rotated. The interfaces between blocks are modeled by the penalty method [Shi (1988)]. The interactions along the interfaces are described as the contacts between block vertices and block edges. Contact springs may be applied in the normal and shear directions at each vertex-edge contact position according to the contact status, which can be open, sliding, or locked. The DDA solution follows a time marching schedule, i.e., force or displacement loadings can be applied by time step. In each time step, open-close iterations are executed to enforce the penetrations between blocks to be smaller than the allowable value, which is related to the user-supplied maximum step displacement ratio, and to ensure no tensions between blocks; meanwhile, the Mohr-Coulomb failure criterion can also be employed for block interactions. Within such a procedure, the interfaces between blocks can be closed, opened, and slipped. A running flow chart of the DDA program is given in Fig. 1. The behaviors of the blocks and the interfaces in the DDA are very similar to that of the rock blocks and the joints in a jointed rock mass; therefore, the DDA is especially suitable for modeling the mechanical behaviors of jointed rock masses. Under time-dependent force or displacement loadings, DDA blocks will be deformed and moved, which result in the deformation of the interfaces between blocks. In the modeling of wave propagations in a jointed rock mass, the dynamic excitations are thus spread to the far region. Obviously, the attenuations and propagating velocities of the stress waves depend on the properties of the rock blocks as well as of the interfaces/joints between blocks.

It is commonly recognized that the mesh/element size of a numerical model influences the modeling accuracy remarkably for dynamic problems, whether a continuum- or discontinuum-based numerical method is used. In the FEM, Kuhlmeier and Lysmer (1973) recommended a mesh ratio, defined as the ratio between the maximum element length along the wave propagation direction and the minimum wavelength, smaller than 1/8 - 1/12 for accurate modeling one-dimensional wave propagations. In the DDA with first-order displacement functions, each block is in a constant stress/strain state. In the modeling of wave propagations with the DDA, the block size was also proved to be one of the major factors influencing the simulation accuracy [Gu and Zhao (2009)], and the proposed block ratio, defined similarly to the element ratio in the FEM, is smaller than 1/16.

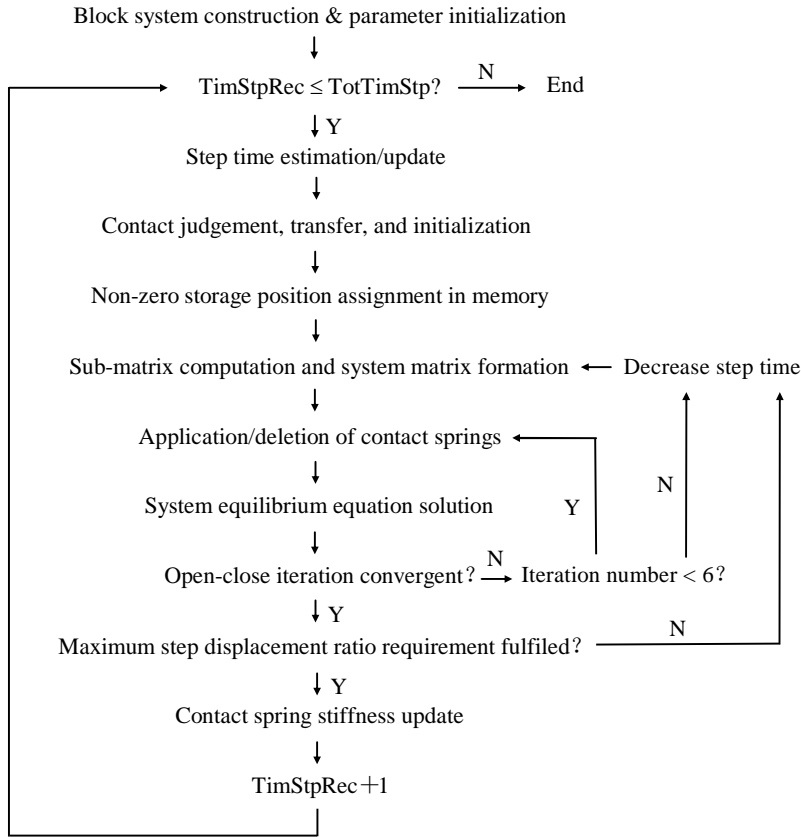


Figure 1: Running flow chart of DDA program

Using the DDA, it was proved as well that the decrease of the step time can help to improve the accuracy of the numerically derived peak values of the propagating stress waves [Gu and Zhao (2009); Bao, Hatzor, and Huang (2012)]; however, the decrease of the step time means the decrease of the computational efficiency simultaneously. The suitable step time  $\Delta t$  was recommended to be selected by the following formulas:

$$\Delta t^a = a \min(h_{\min}/C_P) \quad (1)$$

$$\Delta t^b = 2b \sqrt{m_{\min}/K_{\max}} \quad (2)$$

$$\Delta t < \min(\Delta t^a, \Delta t^b) \quad (3)$$

where  $\Delta t^a$  accounts for the internal block system [Chen (1999)], and  $C_P$  is the P-wave velocity,  $h_{\min}$  is the minimum height of the blocks, and  $a$  is a user-supplied

factor to account for the increase of apparent stiffness due to the contact springs attached to the boundary zones;  $\Delta t^b$  accounts for the contacts between blocks [Last and Harper (1990)], and  $m_{\min}$  is the mass of the smallest block in the system,  $K_{\max}$  is the maximum contact stiffness, and  $b$  is a user-supplied factor to account for the case in which a block may be contacted with several blocks. In the DDA calculation, the user-supplied upper limit of step time  $g1$  can be selected based on the smaller one of  $\Delta t^a$  and  $\Delta t^b$ . In each time step, the step time will be adjusted to a smaller value automatically by the DDA code when necessary to fulfill the infinitesimal displacement/deformation assumption within one time step, which is controlled by the user-supplied maximum step displacement ratio, and to achieve the convergence of contact statues at all the contact positions in the open-close iterations, as illustrated in Fig. 1.

In rock mechanics, the stiffness of a rock joint is defined as the ratio of the incremental change in stress across the joint to the incremental joint closure induced by the corresponding stress [Cook (1992)]. In the DDA, two vertex-edge contacts exist at the two ends of an interface/joint between two edge-to-edge contacted blocks, respectively. The normal joint stiffness  $k_n$  in DDA models can be calculated as

$$k_n = \frac{\Delta\sigma_n}{\Delta x_n} = \frac{2f_n/l_0}{\Delta d_n} = \frac{2(g0 \times \Delta d_n)/l_0}{\Delta d_n} = \frac{2g0}{l_0} \quad (4)$$

where  $\Delta\sigma_n$  and  $\Delta x_n$  are the change of the stress across a joint and the joint deformation normal to the joint surfaces, respectively;  $l_0$  is the joint length;  $f_n = g0 \times \Delta d_n$  is the normal contact force at each vertex-edge contact, and  $g0$  is the normal contact spring stiffness in the penalty method,  $\Delta d_n$  is the normal contact displacement. Here, it is assumed that the two half spaces of a joint have parallel movements without rotations, thus  $\Delta x_n = \Delta d_n$ . In the DDA code provided by Shi, which is used in this study, the shear contact spring stiffness is set to be 2/5 times of the normal contact spring stiffness. Similarly, the shear joint stiffness  $k_s$  can be approximated as

$$k_s = \frac{\Delta\sigma_s}{\Delta x_s} = \frac{2}{5} \times \frac{\Delta\sigma_n}{\Delta x_n} = \frac{4g0}{5l_0} = 0.4k_n \quad (5)$$

Obviously, the normal and shear joint stiffness are proportional to the applied normal contact spring stiffness.

## 2.2 Wave propagations in jointed rock bars

In the DDA with first-order displacement functions, the stress/strain in each block is a constant. In order to capture the deformation behavior of a rock mass with acceptable accuracy for wave propagation analysis, the block size should be small enough.

Due to this restriction, the first-order DDA, without further internal discretization, can only be applied in the modeling of wave propagations in rock masses consisting of enough-small blocks as compared with the wavelength.



(a) Model 1, inclination =  $90^\circ$



(b) Model 2, inclination =  $60^\circ$



(c) Model 3, inclination =  $30^\circ$

Figure 2: Three jointed rock bars with different inclinations of the non-horizontal joint set

### 2.2.1 Model descriptions

Three jointed rock bar DDA models, as shown in Fig. 2, are constructed to investigate the one-dimensional P-wave propagations. The length and height of the bars are  $L = 20.0$  m and  $H = 1.0$  m, respectively. Two joint sets are included in each bar. In Model 1, the two joints sets lie horizontally and vertically, respectively. In Model 2, the non-horizontal joint set has an inclination of  $60^\circ$  to the horizontal joints, and in Model 3, the inclination of the non-horizontal joint set is  $30^\circ$ . The joint spacing/block size in all the three models is consistent as  $l = 0.2$  m. The mass density, Young's modulus, and Poisson's ratio of the rock blocks are  $\rho = 2000$  kg/m<sup>3</sup>,  $E = 50$  GPa, and  $\mu = 0.25$ , respectively. Time-dependent dynamic loadings are applied at the left ends. The right ends of the bars are set as totally fixed boundaries. The large length-width ratio ( $L/H = 20$ ) of the rock bars ensure to a large extent that there is negligible geometrical damping for the one-dimensional wave propagations. With linear elastic properties of the rock blocks, theoretically, the propagations of the stress waves in the rock bars will only be attenuated by the effects of the joints as compared with the one-dimensional wave propagations in intact rock medium. The P-wave velocity in the intact rock can be calculated to be  $C_P = 5000$  m/s according to the density and Young's modulus of the rock blocks. With a joint spacing/block size of 0.2 m, in order to satisfy the proposed block ratio,

smaller than 1/16, required for wave propagation modeling, in these DDA models, the minimum wavelength and the maximum frequency of the seismic loading that can be accounted for are 3.2 m and 1562.5 Hz, respectively.

In the three models, the minimum height of the blocks is  $h_{\min} = 0.2$  m, then  $\Delta t^a$  in Eq. (1) can be calculated as  $\Delta t^a = 4 \times 10^{-5}a$ . The mass of the smallest block is  $m_{\min} = 80$  kg. In the modeling of wave propagations in the rock bars, the maximum normal contact spring stiffness in the penalty method will be  $g_0 = 50E$ , i.e., in Eq. (2),  $K_{\max} = 50E$ , where  $E$  is the Young's modulus, then  $\Delta t^b$  can be calculated as  $\Delta t^b = 1.13 \times 10^{-5}b$ . Based on these calculations, the upper limit of step time is selected to be  $g_1 = 2 \times 10^{-6}$  s in the DDA modeling, thus  $a$  is evaluated to be 0.05 from Eq. (1), and  $b$  is evaluated to be 0.177 from Eq. (2). The dynamic parameter, defined as the inherited block velocity proportion from one time step to the next time step, is chosen as  $gg = 1$ , i.e., fully dynamic calculation is used. The maximum step displacement ratio, defined as the ratio between the allowable step maximum displacement for all the points in the calculation domain to the half length of the calculation domain in the Y direction, is chosen as  $g_2 = 0.005$ , according to Shi's DDA user's manual. With these numerical control parameters, it is found that in all the DDA modeling examples of wave propagations in the rock bars, the step time does not change automatically in the open-close iteration process throughout the calculations, which indicates that the given upper limit of step time is small enough to fulfill the infinitesimal deformation assumptions in each time step that is restricted by the given maximum step displacement ratio.

### 2.2.2 Effect of joint stiffness

When stress waves propagate through an elastic joint, the stress across the joint is continuous and the displacement across the joint is discontinuous. For a displacement discontinuity, both the amplitude and phase of the transmitted and reflected waves depend on the ratio of the joint stiffness to the seismic impedance and on the frequency [Cook (1992)]. As one of the key factors influencing wave propagations through joints, the joint stiffness is investigated in the DDA modeling first. In these modeling examples, one period of a sinusoidal seismic loading with a peak value of 5 MPa and a frequency of 1000 Hz is applied in Model 1. The friction angle, cohesion, and the tensile strength of the rock joints are  $\varphi = 40^\circ$ ,  $c = 8$  MPa, and  $\sigma_t = 8$  MPa, respectively. Here, a complete period of sinusoidal loading is applied to verify the DDA's capability in modeling compressive stress wave as well as tensile stress wave propagations. A real rock joint always has a very low tensile strength. A tensile stress wave with relatively high intensity will lead to the opening of the joint interface and the wave amplitude will be attenuated to zero very soon. In these DDA modeling examples, a large joint tensile strength of 8 MPa is used to ensure no

failures of the joints under the tensile loading and thus ensure the propagations of the tensile stress waves through the block interfaces. The value of the joint tensile strength will not affect the propagations of the compressive stress waves through the joints because the joints will be compressed under compressive loadings. In the modeling, five different values of the normal contact spring stiffness in the penalty method are used, and the horizontal stress time histories at the center of the bar are plotted in Fig. 3.

In Model 1, the joints between all the edge-to-edge contacted blocks have a length of  $l_0 = 0.2$  m. According to Eqs. (4) and (5), the normal and shear joint stiffness can be derived as  $10g_0$  and  $4g_0$ , respectively. As shown in Fig. 3, with the increase of the contact spring stiffness/joint stiffness, the stress wave amplitude attenuates slower with a higher propagating velocity. These phenomena are consistent with the general recognition of the effects of joint stiffness on stress wave propagations. When the joint stiffness approaches infinitely, the interface becomes a welded boundary [Zhao, Zhao, and Cai (2006)], and the transmitted wave is essentially identical to the incident wave. In the DDA modeling, when  $g_0$  is larger than  $20E$ , further increase in  $g_0$  no longer affects the modeling results obviously. Almost the same results are obtained when  $g_0$  is evaluated as  $20E$  and  $50E$ . When  $g_0 = 20E$ , taking point A in Fig. 3 as reference, the velocity of the stress wave propagating from the left end to the middle of the bar is calculated to be 4999.994 m/s, which is very close to that in the intact rock. The wave amplitude at point A is 4.891 MPa, attenuated 2.18% after propagating a two-wavelength distance (10 m, half length of the bar). With high contact spring stiffness/joint stiffness, the wave velocity is nearly not affected by the joints; however, the wave amplitude still encounters some attenuation. One possible reason is that even if high contact spring stiffness is used in the model, minor penetrations between blocks still exist in the penalty method, and the joints are not really welded, thus the amplitude attenuations still appear. The stress wave amplitude attenuations may also be attributed to the geometrical damping due to the model geometry and the boundary conditions applied. When  $g_0 = E$ , the corresponding stress wave velocity is 4081.63 m/s and the attenuated proportion of the wave amplitude is 6.12%. The amplitude attenuation and time delay effects of rock joints on the propagations of stress waves are well manifested by the DDA modeling.

### 2.2.3 Effect of seismic frequency

The attenuation effects of rock joints on the stress waves are characterized by both decreasing the amplitude and filtering the high frequency components [Pyrak-Nolte, Myer, and Cook (1990a)], which means that the effect of rock joints on stress wave amplitude attenuations increases with the increase of frequency. Again, si-

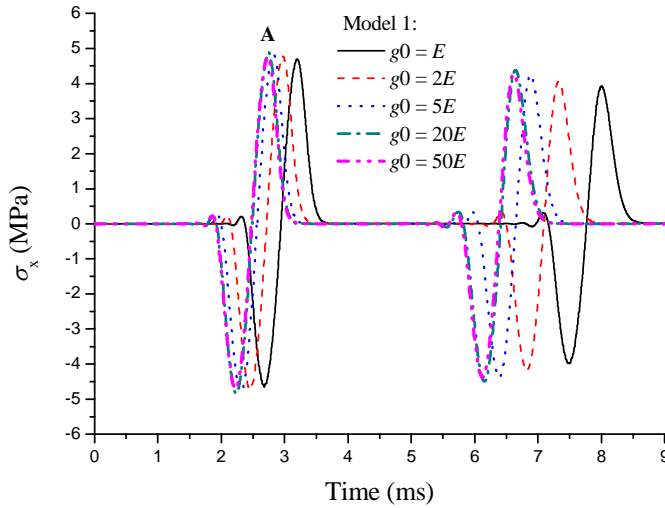


Figure 3: Influence of contact spring stiffness in the DDA on stress wave propagations

nusoidal seismic loadings of one complete period with a peak value of 5 MPa and three different values of the frequency are applied in rock bar Model 1. The joint strength used is the same as that used in the previous modeling examples. The normal contact spring stiffness in the penalty method is selected to be  $g_0 = E$ . The horizontal stress time histories at the center of the bar are plotted in Fig. 4. Obviously, the stress wave amplitude attenuates faster with the increase of the frequency. Under the three frequencies, namely, 500 Hz, 1000 Hz, and 1500 Hz, the first arriving tensile stress wave peak value is 4.790 MPa, 4.694 MPa, and 4.246 MPa, respectively (point A, B, and C in Fig. 4, respectively). The attenuation proportions are 4.20%, 6.12%, and 15.08%, respectively. On the other hand, the DDA modeling results also indicate that the influence of seismic loading frequency on the velocity of the stress wave propagations is not evident.

#### 2.2.4 Effects of joint strength and direction

In the above modeling examples, relatively high joint cohesion and tensile strength are used to guarantee no failures taking place in the joint interfaces according to the Mohr-Coulomb failure criterion. Under certain conditions, for example, in the near region of a blasting source, the joint strength may not be able to bear the relatively high loading intensity, and the rock joints will be opened and/or slipped. The wave propagations in such problems may differ greatly from those in a rock mass with persistent closed joints. Here, DDA modeling examples are carried out

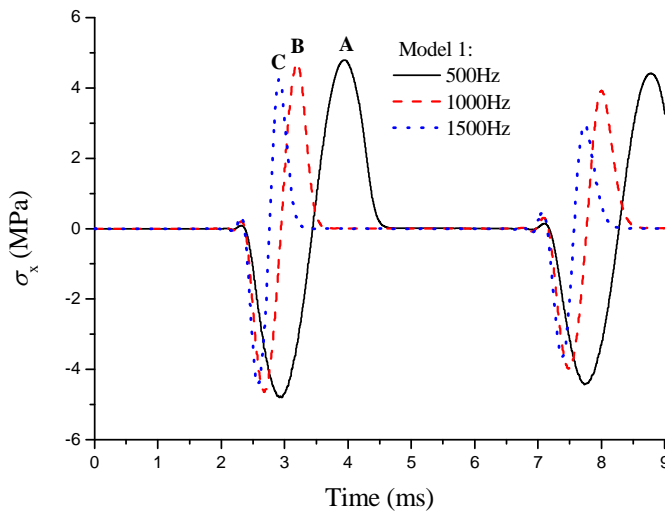


Figure 4: Influence of seismic frequency on stress wave propagations

to investigate the wave propagations in a jointed rock mass with relatively low joint strength as compared with the seismic loading intensity. Three levels of joint strength as listed in Table 1 will be used in the modeling. Since under tensile seismic loadings with relatively high amplitudes, a rock joint will be opened and the transmitted wave will be zero, in these modeling examples, only a half period sinusoidal compressive pressure with a peak value of 5 MPa and a frequency of 1000 Hz is applied to Model 1 and Model 2. In joint strength level 1, in which a high value of 8 MPa is evaluated to the cohesion and the tensile strength, respectively, the corresponding modeling results are to be used to compare with the results under the other two strength levels. In joint strength levels 2 and 3, the cohesion and the tensile strength are smaller than the peak value of the seismic loading. The normal contact spring stiffness in the penalty method is selected to be  $g_0 = E$ .

Table 1: Different joint strength for rock bars

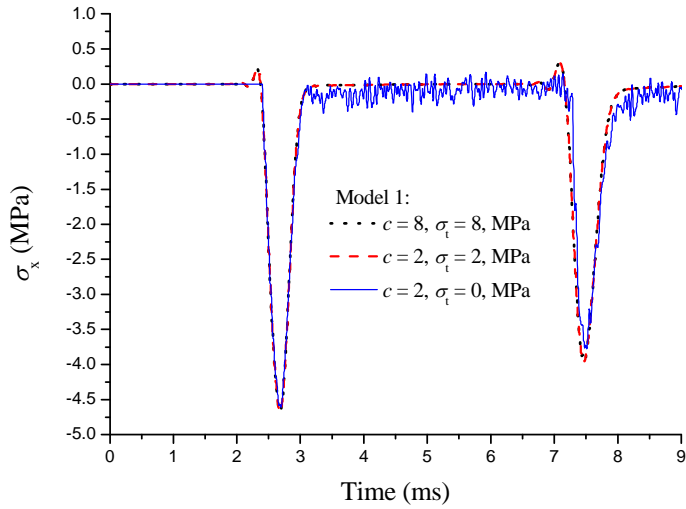
Strength level	Friction angle ( $\varphi / ^\circ$ )	Cohesion ( $c$ /MPa)	Tentle strength ( $\sigma_t$ /MPa)
1	40	8	8
2	40	2	2
3	40	2	0

Fig. 5 shows the horizontal stress time histories at the center of rock bar Model 1 and Model 2 under three different levels of joint strength. It can be found that the

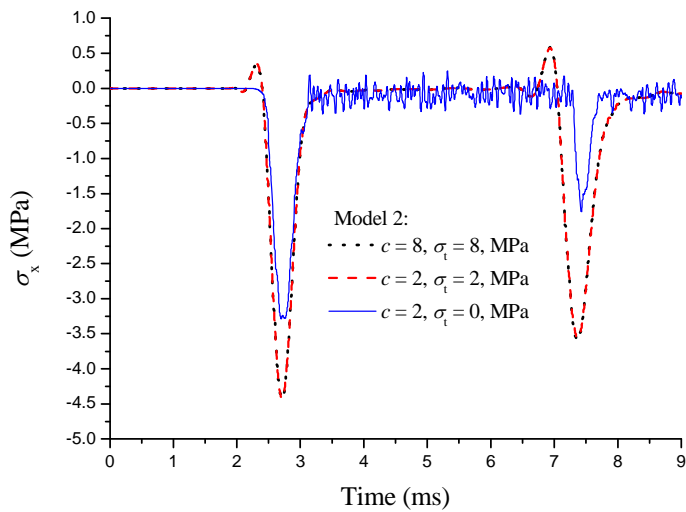
decrease of the joint cohesion  $c$  and tensile strength  $\sigma_t$  does not affect the propagations of the compressive stress waves in Model 1 remarkably. In Model 2, joint strength levels 1 and 2 almost lead to the same wave propagation result, which indicates that when  $c = 2$  MPa and  $\sigma_t = 2$  MPa, few failures take place in the joints; however, when  $c = 2$  MPa and  $\sigma_t = 0$ , the stress wave amplitude is cut off to a obviously smaller value (3.29 MPa at the first peak and 1.76 MPa at the second peak) as compared with that under the joint strength level 1 (4.43 MPa at the first peak and 3.58 MPa at the second peak). Meanwhile, when  $c = 2$  MPa and  $\sigma_t = 0$ , fibrillations appear in the propagations of the stress waves in both of the two models.

In Model 1, the vertical joint set is perpendicular to the propagating direction of the one-dimensional compressive P-waves. The low strength of these joints has no influence on the wave propagations as compared with the high joint strength because the joints will not be opened or slipped under the compressive loadings. Under the three levels of joint strength, almost the same stress propagation results, except the fibrillations when  $c = 2$  MPa and  $\sigma_t = 0$ , are obtained, which indicates that the strength of the horizontal joint set also has negligible influence on the propagations of the stress waves as well. This result is consistent with the recognized conclusion that when the joints are parallel to the stress wave propagating directions, the joints have little influence on the wave propagations [Cook (1992); Lei, Hefny, Yan, and Teng (2007); Zhang, Wong, Wang, and Han (2011)]. In Model 2, when  $c = 2$  MPa and  $\sigma_t = 0$ , the zero tensile strength of the horizontal joints makes it possible for the rock blocks to move along the direction of the inclined joint set, and the inclined joints may thus be slipped. The cutoff of the stress wave amplitude is induced by such slip of the inclined joints under the low joint strength. The amplitude cutoff phenomenon in stress wave propagations through slippery joints was also reported by Li, Ma, and Zhao (2011a). Under a low joint strength, the joints may be opened and/or slipped and the rock blocks may thus be excited and vibrated, hence, a boarder frequency band of the stress waves are generated and fibrillations appear in the wave propagations. The fibrillation phenomenon was also reported in UDEC modeling of wave propagations in jointed rock masses by Fan, Jiao, and Zhao (2004). As compared with wave propagations in a continuous model, the frequency band of the wave may be of a wider range while propagating in a jointed mass [Ma, Hao, and Zhou (1998)].

As revealed by the above modeling examples, the propagations of stress waves are affected by the joint strength as well as the joint direction, or, more precisely, the stress wave incident angles to the joints. A half period sinusoidal compressive pressure with a peak value of 5 MPa and a frequency of 1000 Hz is applied, respectively, to the three rock bar models in Fig. 2. The cohesion and tensile strength of the joints are both 2 MPa and the friction angle is  $40^\circ$ . The normal contact spring



(a) Model 1



(b) Model 2

Figure 5: Influence of joint strength on stress wave propagations

stiffness in the penalty method is selected to be  $g_0 = E$ . The horizontal stress time histories at the center of the bars are plotted in Fig. 6. It can be found that, with the decrease of the inclination angle of the non-horizontal joint set, i.e., the increase of the incident angle of the seismic loading to the non-horizontal joints, the propagating velocity of the stress wave increases; however, the wave amplitude is attenuated much faster. Under seismic loadings, the occurrence of the relative slip of a joint is related to the incident angle of the seismic loadings to the joint [Li, Ma, and Zhao (2011a)]. The increase of the incident angle of the seismic loading to the non-horizontal joints from Model 1 to Model 3 benefits the slip of the joints, and thus the wave velocity is increased and the wave amplitude is attenuated more severely.

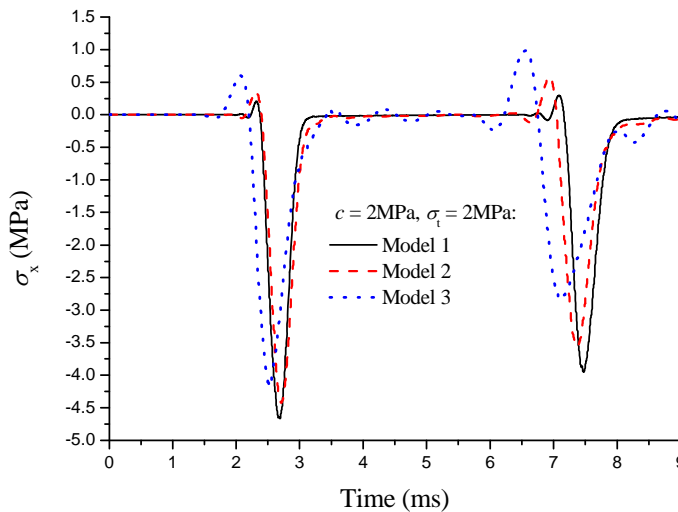


Figure 6: Influence of joint direction on stress wave propagations

### 3 Two nonreflecting boundary conditions in the DDA

In the numerical modeling of seismic response of rock slopes, landslides, or underground structures, and in the modeling of rock blasting problems, fictitious boundaries are always used in a calculation model because the real physical domain is infinite in nature while the calculation domain that can be considered is finite. To avoid the effect of the reflected energy from the fictitious boundaries on the simulation results, large-enough models could be constructed; however, an unreasonably long computer run-time may thus be required. Alternatively, nonreflecting artificial boundaries can be employed to absorb the reflections from the fictitious

boundaries. By virtue of nonreflecting boundaries, a relatively small calculation model may be applicable and the computer run-time can be reduced effectively. Jiao, Zhang, Zhao, and Liu (2007) and Gu and Zhao (2009) introduced a viscous nonreflecting boundary condition (VBC) in the DDA. Ning et al. [Ning, Yang, Ma, and Chen (2009); Ning, Yang, An, and Ma (2011); Ning, Yang, Ma, and Chen (2011)] applied this boundary condition in their rock blasting models. Bao, Hatzor, and Huang (2012) further developed this VBC in the DDA and got better absorbing ability. In this paper, another modified VBC and a new nonreflecting boundary, namely, the superposition boundary condition (SBC), for the DDA is introduced. The applicability of these two boundary conditions is to be investigated and compared.

### 3.1 Viscous boundary condition (VBC)

The viscous nonreflecting boundary algorithm was first proposed by Lysmer and Kuhlemeyer (1969), in which viscous dashpots are placed at artificial boundaries to absorb the stress wave reflections. This boundary model is independent of wave frequency, thus harmonic and non-harmonic waves can be absorbed. In the DDA, a pair of independent dashpots is applied in the normal and shear directions, respectively, at each end of a block edge within the nonreflecting boundaries. For a pair of dashpots at point (x,y), the viscous normal and shear tractions are calculated as [Jiao, Zhang, Zhao and Liu (2007)]

$$t_n = -\rho C_p v_n, t_s = -\rho C_s v_s \tag{6}$$

respectively, where  $\rho$  is the mass density of the block; ( $v_n, v_s$ ) are the normal and shear velocities at point (x,y);  $C_p = \sqrt{(K + 4G/3)/\rho}$  and  $C_s = \sqrt{G/\rho}$  are the P-wave and S-wave velocities, respectively, and  $K$  and  $G$  are the bulk modulus and shear modulus of the block material, respectively. The viscous forces supplied by a pair of dashpots are then obtained as

$$\begin{pmatrix} f_n \\ f_s \end{pmatrix} = \frac{l}{2} \begin{pmatrix} t_n \\ t_s \end{pmatrix} = -\frac{\rho l}{2} \begin{pmatrix} C_p & 0 \\ 0 & C_s \end{pmatrix} \begin{pmatrix} v_n \\ v_s \end{pmatrix} = -\frac{\rho l}{2} \begin{pmatrix} C_p & 0 \\ 0 & C_s \end{pmatrix} \begin{pmatrix} n_x & n_y \\ -n_y & n_x \end{pmatrix} \begin{pmatrix} v_x \\ v_y \end{pmatrix} \tag{7}$$

where  $l$  is the length of the block nonreflecting edge; ( $v_x, v_y$ ) are the velocities at point (x,y) in the x and y directions; ( $n_x, n_y$ ) are the direction cosines of the edge. Here, it is assumed that each pair of dashpots affords half length of an edge to absorb the reflected energy, thus a half edge length  $l/2$  is used in the equation.

The potential energy of a pair of dashpots is then derived as

$$\Pi_v = - \begin{pmatrix} u_n & u_s \end{pmatrix} \begin{pmatrix} f_n \\ f_s \end{pmatrix} = - \begin{pmatrix} u_x & u_y \end{pmatrix} \begin{pmatrix} n_x & -n_y \\ n_y & n_x \end{pmatrix} \begin{pmatrix} f_n \\ f_s \end{pmatrix} \tag{8}$$

where  $(u_n, u_s)$  are the normal and shear displacements at point  $(x, y)$ , and  $(u_x, u_y)$  are the displacements in the  $x$  and  $y$  directions. Substituting Eq. (7) into Eq. (8), we have

$$\Pi_v = \frac{\rho l}{2} (u_x \quad u_y) \begin{pmatrix} C_p n_x^2 + C_s n_y^2 & (C_p - C_s) n_x n_y \\ (C_p - C_s) n_x n_y & C_s n_x^2 + C_p n_y^2 \end{pmatrix} \begin{pmatrix} v_x \\ v_y \end{pmatrix} = \frac{\rho l \mathbf{D}_i^T \mathbf{T}_i^T \mathbf{C} \mathbf{T}_i \dot{\mathbf{D}}_i}{2} \quad (9)$$

where  $i$  is block index in a block system;  $\mathbf{D}_i$  and  $\mathbf{T}_i$  are the deformation variable matrix and the displacement transformation matrix for block  $i$ , respectively. Considering the initial condition, the velocity term can be written as [Shi (1988)]

$$\dot{\mathbf{D}}_i = \frac{\mathbf{D}_i - \mathbf{D}_{i0}}{\Delta} = \frac{\mathbf{D}_i}{\Delta} \quad (10)$$

where  $\Delta$  is the step time. Substituting Eq. (10) into Eq. (9),  $\Pi_v$  is further expressed as

$$\Pi_v = \frac{\rho l \mathbf{D}_i^T \mathbf{T}_i^T \mathbf{C} \mathbf{T}_i \mathbf{D}_i}{2\Delta} \quad (11)$$

Minimizing this potential energy by taking the derivatives with respect to  $\mathbf{D}_i$ , a  $6 \times 6$  sub-matrix  $\mathbf{K}_{vi}$  is obtained and added into the coefficient matrix of the DDA simultaneous equilibrium equations:

$$\mathbf{K}_{vi} = \frac{\rho l \mathbf{T}_i^T \mathbf{C} \mathbf{T}_i}{\Delta} \rightarrow \mathbf{K}_{ii} \quad (12)$$

where  $\mathbf{K}_{ii}$  is the coefficient sub-matrix for block  $i$ . In the papers by Jiao, Zhang, Zhao, and Liu (2007), Gu and Zhao (2009), and Ning, Yang, Ma, and Chen (2009), a whole edge length  $l$  is used for each pair of dashpots in the derivation of the viscous forces in Eq. (7), thus their derived sub-matrix  $\mathbf{K}'_{vi}$  is two times of  $\mathbf{K}_{vi}$ . In the paper by Bao, Hatzor, and Huang (2012), the authors also proved that  $\mathbf{K}'_{vi}$  is around two times of their derived sub-matrix  $\mathbf{K}''_{vi}$ . This indicates that the modified VBC in this paper is nearly equivalent to the VBC further developed by Bao, Hatzor, and Huang (2012), thus good absorbing ability can be expected when this modified VBC is used.

### 3.2 Superposition boundary condition (SBC)

The superposition nonreflecting boundary algorithm was originally proposed by Smith (1974) based on the principle of virtual images, and this model is independent of the wave frequency as well as the wave incident angle. The SBC procedure entails computing the dynamic solution with at least two different boundary conditions: first with the normal displacements and tangential stresses at the boundaries

equal to zero, then with the normal stresses and tangential displacements equal to zero. These two solutions are then averaged. In the DDA, the above two solutions are added as two boundary value problems [Qian (2008); Ning (2008)]. Boundary value problem I has the following boundary conditions:

$$u_x = 0, \sigma_y = 0 \tag{13}$$

where  $u_x$  and  $\sigma_y$  are the displacement and stress at point  $(x,y)$  on the boundary in the x and y directions, respectively. The two boundary conditions in Eq. (13) correspond to the Dirichlet problem for  $u_x$  and the Neumann problem for  $u_y$ , respectively. For boundary value problem II, we have

$$\sigma_x = 0, u_y = 0 \tag{14}$$

where  $\sigma_x$  and  $u_y$  are the stress and displacement at point  $(x,y)$  on the boundary in the x and y directions, respectively. The two boundary conditions in Eq. (14) correspond to the Dirichlet problem for  $u_y$  and the Neumann problem for  $u_x$ , respectively. According to the principle of virtual images, reflections from the fictitious boundaries of a model are expected to be eliminated by superposing the above Dirichlet and Neumann problems.

The two boundary value problems in Eqs. (13) and (14) are applied at two ends of each block edge within the nonreflecting boundaries in the DDA. For boundary value problem I, a spring with stiffness  $p_0$  is used to fulfill the zero displacement constraint in the x direction. The spring force in the x direction and the resistance force in the y direction are

$$f_x = -p_0u_x, f_y = -\rho l\sigma_y = 0 \tag{15}$$

respectively, where  $\rho$  is the mass density of the block;  $l$  is the length of the block nonreflecting edge. The potential energy of boundary value problem I is then calculated as

$$\begin{aligned} \Pi_I &= - \begin{pmatrix} u_n & u_s \end{pmatrix} \begin{pmatrix} f_n \\ f_s \end{pmatrix} = - \begin{pmatrix} u_x & u_y \end{pmatrix} \begin{pmatrix} n_x & -n_y \\ n_y & n_x \end{pmatrix} \begin{pmatrix} n_x & n_y \\ -n_y & n_x \end{pmatrix} \begin{pmatrix} f_x \\ f_y \end{pmatrix} \\ &= - \begin{pmatrix} u_x & u_y \end{pmatrix} \begin{pmatrix} n_x^2 + n_y^2 & 0 \\ 0 & n_x^2 + n_y^2 \end{pmatrix} \begin{pmatrix} f_x \\ f_y \end{pmatrix} \\ &= - \begin{pmatrix} u_x & u_y \end{pmatrix} \begin{pmatrix} f_x \\ f_y \end{pmatrix} \end{aligned} \tag{16}$$

where  $(u_n, u_s)$  are the normal and shear displacements;  $(f_n, f_s)$  are the normal and shear resistance forces;  $(n_x, n_y)$  are the direction cosines of the block nonreflecting edge. Substituting Eq. (15) into Eq. (16), we have

$$\Pi_I = - \begin{pmatrix} u_x & u_y \end{pmatrix} \begin{pmatrix} -p_0u_x \\ 0 \end{pmatrix} \tag{17}$$

Similarly, for boundary value problem II, a constraint spring with stiffness  $p_0$  is applied in the y direction. The resistance force in the x direction and the spring force in the y direction are

$$f_x = -\rho l \sigma_x = 0, f_y = -p_0 u_y \quad (18)$$

respectively. Then, the potential energy can be derived as

$$\Pi_{II} = - \begin{pmatrix} u_x & u_y \end{pmatrix} \begin{pmatrix} 0 \\ -p_0 u_y \end{pmatrix} \quad (19)$$

Eqs. (17) and (19) are then averaged to obtain the final solution for the superposition nonreflecting boundary condition:

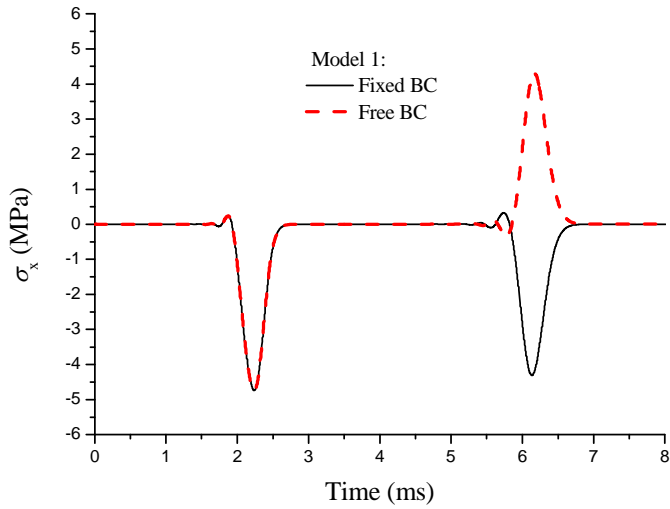
$$\begin{aligned} \Pi_s &= \frac{1}{2} (\Pi_I + \Pi_{II}) = \frac{p_0}{2} \begin{pmatrix} u_x & u_y \end{pmatrix} \begin{pmatrix} u_x \\ 0 \end{pmatrix} + \frac{p_0}{2} \begin{pmatrix} u_x & u_y \end{pmatrix} \begin{pmatrix} 0 \\ u_y \end{pmatrix} \\ &= \frac{p_0}{2} \begin{pmatrix} u_x & u_y \end{pmatrix} \begin{pmatrix} u_x \\ u_y \end{pmatrix} \\ &= \frac{p_0}{2} \mathbf{D}_i^T \mathbf{T}_i^T \mathbf{T}_i \mathbf{D}_i \end{aligned} \quad (20)$$

where  $i$  is block index in a block system. Minimizing this potential energy by taking the derivatives with respect to  $\mathbf{D}_i$ , a  $6 \times 6$  sub-matrix  $\mathbf{K}_{si}$  is obtained and added to the coefficient matrix of the DDA simultaneous equilibrium equations:

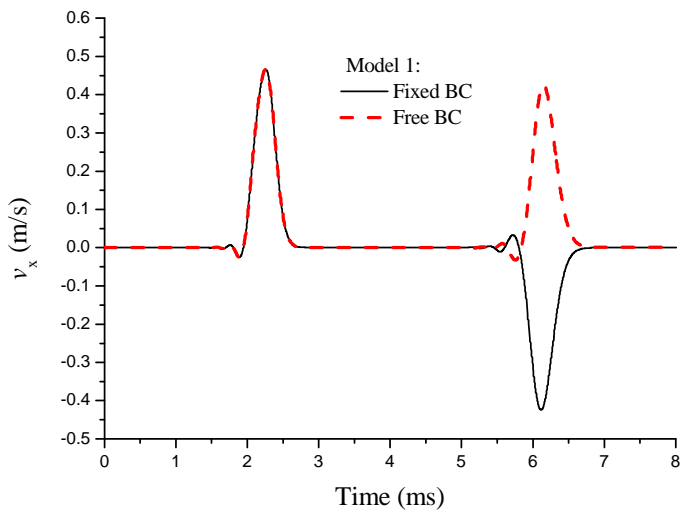
$$\mathbf{K}_{si} = p_0 \mathbf{T}_i^T \mathbf{F} \mathbf{T}_i \rightarrow \mathbf{K}_{ii} \quad (21)$$

### 3.3 Absorbing ability to one-dimensional P-waves

The original DDA possesses two boundary conditions, i.e., the totally fixed boundary condition (Fixed BC) and the free boundary condition (Free BC). Fig. 7 shows the horizontal stress and particle velocity time histories at the center of rock bar Model 1 in Fig. 2 when the right end of the bar is set as the Fixed BC and the Free BC, respectively, in which a half period sinusoidal compressive pressure with a peak value of 5 MPa and a frequency of 1000 Hz is applied at the left end of the bar. In the DDA modeling in this section, the normal contact spring stiffness in the penalty method is selected to be  $g_0 = 50E$ ; the strength of the joints in the rock bars is selected to be  $40^\circ$  for the friction angle and 8 MPa for the cohesion and the tensile strength, respectively. Other numerical control parameters and the rock block properties are selected to be the same as that used in Section 2. As shown in Fig. 7, after the reflection at the right end of the model, the sign of the stress keeps unchanged under the Fixed BC and is inverted under the Free BC with the same amplitude of 4.45 MPa at the center of the bar, while the sign of the particle



(a) stress



(b) particle velocity

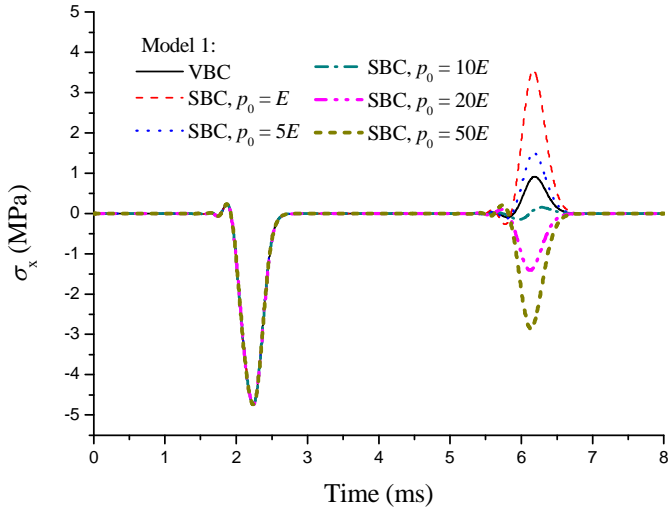
Figure 7: Fixed BC and Free BC in the DDA

velocity keeps unchanged under the Free BC and is inverted under the Fixed BC with the same amplitude of 0.424 m/s at the center of the bar. For the modeling of a dynamic problem in an infinite media, the reflections at the artificial boundaries of a finite model will distort the modeling results due to the reflections at the boundaries if the Fixed BC or the Free BC is used.

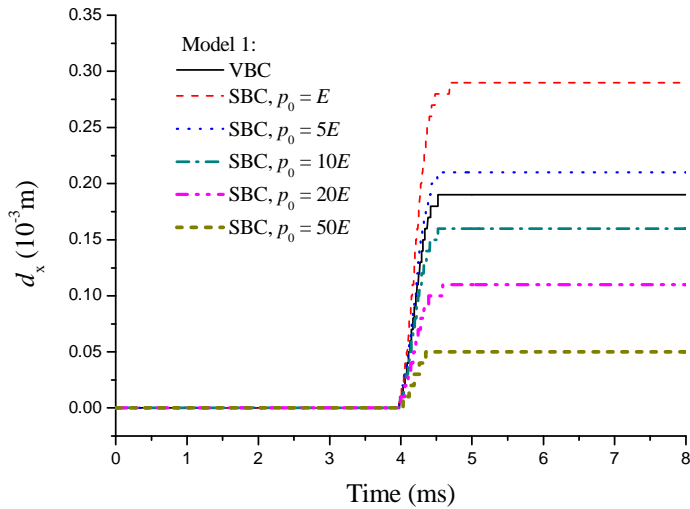
### 3.3.1 Influence of constraint spring stiffness in the SBC

For the same stress wave propagation problem above, Fig. 8a shows the stress time histories at the center of the bar when the right end of the bar is set as the VBC and the SBC with different constraint spring stiffness,  $p_0$ . With the VBC, the amplitude of the reflected stress wave at the center of the bar is 0.945 MPa, 78.77% absorbed as compared with that under the Fixed BC or the Free BC. The absorbing ability of the SBC varies with different values for  $p_0$ . When  $p_0$  is relatively small, the SBC behaves close to the Free BC, i.e., a tensile reflected stress wave is generated for a compressive input; when  $p_0$  is relatively large, the SBC behaves close to the Fixed BC. It is noted that the sub-matrix added in the DDA in Eq. (21) is exactly the same as that for a fixed point being added to the coefficient matrix of the DDA simultaneous equilibrium equations by Shi (1988). The difference is that for a fixed point, the constraint spring stiffness is given a very large value as  $100g_0$ , where  $g_0$  is the normal contact spring stiffness in the penalty method and is often chosen to be several to several tens' times of the Young's modulus of the blocks. Moreover, for a fixed point, strong springs are also used to compel the residual displacement at the end of the previous time step to be zero in a new step. With a proper value for  $p_0$ , the reflection can be absorbed by the SBC satisfactorily. In this modeling example, when  $p_0 = 10E$ , the amplitude of the reflected stress wave at the center of the bar is 0.159 MPa, 96.43% absorbed.

When the constraint spring stiffness  $p_0$  is relatively small, the SBC behaves close to the Free BC, thus this boundary condition may not be able to restrict the displacement at the boundary reliably when  $p_0$  is not large enough and a boundary shift problem may be encountered in high loading intensity dynamic problems [Ning (2008)]. In such situations, although the reflections are absorbed to a large extent, the blocks along the boundary are displaced remarkably and their movement will affect the movement of the blocks in the near region where our interests focus. Fig. 8b gives the horizontal displacement time histories at the right end of the bar in the modeling examples. It can be found that with the SBC, the final displacement increases with the decrease of the value of  $p_0$ . When  $p_0 = 10E$ , i.e., when a high absorbing ability is obtained, the displacement is close to that under the VBC. This indicates now the applicability of the SBC is almost equivalent to the VBC. In high loading intensity problems, to achieve a high absorbing ability and to avoid the



(a) absorbing ability



(b) displacement at boundary

Figure 8: VBC and SBC with different constraint spring stiffness

boundary shift problem at the same time, the calculation model could be enlarged to a certain extent thus the loading intensity at the artificial boundaries has been attenuated to a relatively low level.

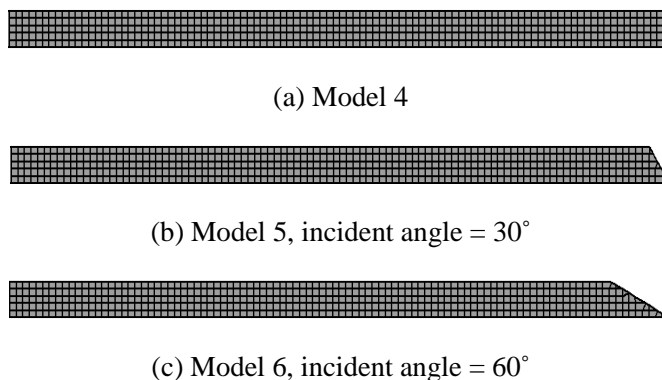


Figure 9: Three jointed rock bars

### 3.3.2 Influences of boundary block edge length and wave incident angle

To further verify the absorbing abilities of the VBC and the SBC, another three jointed rock bar models are constructed as shown in Fig. 9. Model 4 is obtained by merging the five blocks at the right end of Model 1 in Fig. 2 into three blocks with an even height of 0.333 m to check the influence of the boundary block edge length on the absorbing result. It is acknowledged that the incident angle of the seismic loading at the boundary may influence the absorbing ability of a nonreflecting boundary. By changing the inclination of the right end of the bar in Model 1 from  $90^\circ$  to  $60^\circ$  and  $30^\circ$ , respectively, Model 5 and Model 6 are derived. In Model 1, the seismic wave impinges perpendicularly to the right end of the bar, and in Model 5 and Model 6, the incident angle is increased to  $30^\circ$  and  $60^\circ$ , respectively.

Fig. 10 shows the horizontal stress time histories at the center of Model 4, in which a half period sinusoidal compressive pressure with a peak value of 5 MPa and a frequency of 1000 Hz is applied at the left end of the model. With the VBC at the right end, the amplitude of the reflected wave is 0.331 MPa, 92.56% absorbed as compared with that under the Fixed BC or the Free BC, better than that in Model 1. Using the SBC with  $p_0 = 10E$ , the reflected amplitude is 1.184 MPa and the absorbing proportion is 73.39%. To improve the absorbing ability of the SBC, a larger value of  $16E$  for  $p_0$  is used. The reflected amplitude is thus reduced to 0.228

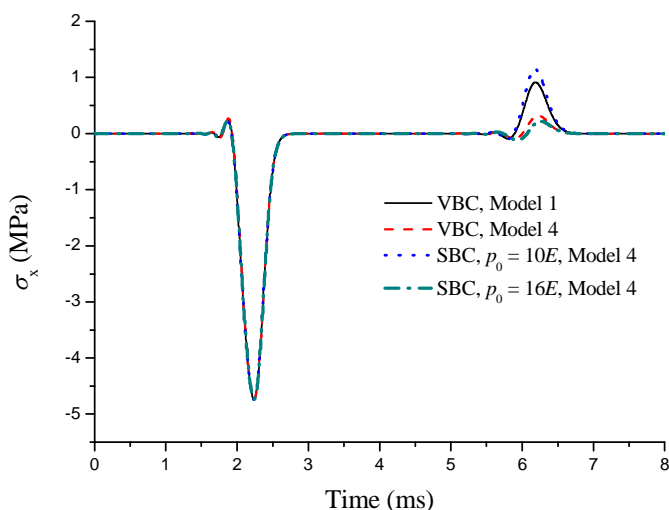


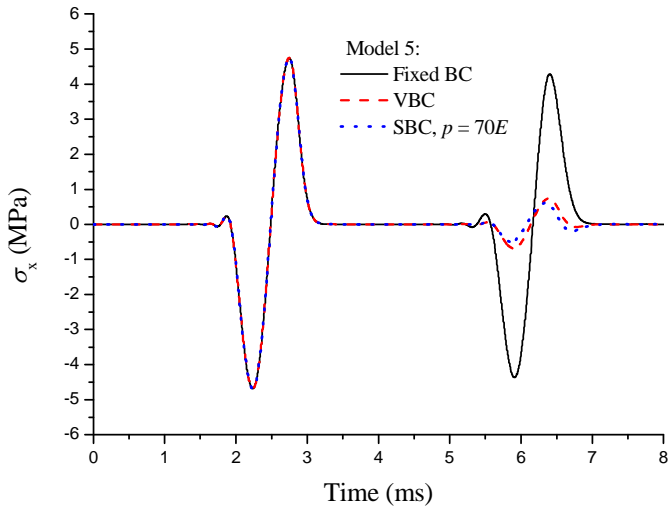
Figure 10: Influence of boundary block edge length on stress wave absorbing ability

MPa and 94.87% of the reflection is absorbed. In Model 1, the boundary block edge length at the right end of the bar is 0.2 m and a value of  $10E$  for  $p_0$  in the SBC brings about a satisfactory absorbing proportion of 96.43%; in Model 4, the boundary block edge length is 0.333 m, 1.67 times of that in Model 1, and a value of  $16E$  for  $p_0$ , 1.6 times of that in Model 1, brings about a close absorbing proportion of 94.87%. It is evident that a larger boundary block edge length requires a larger  $p_0$ , and the increase of both can be deduced to be nearly proportional. This can be easily explained from the point view of energy: a larger constraint spring stiffness is required to absorb a larger amount of the reflected energy from a longer block edge within the nonreflecting boundary under the same loading intensity. To account for the effect of the boundary block edge length on the absorbing ability of the SBC, the sub-matrix added in the DDA in Eq. (21) is further improved as

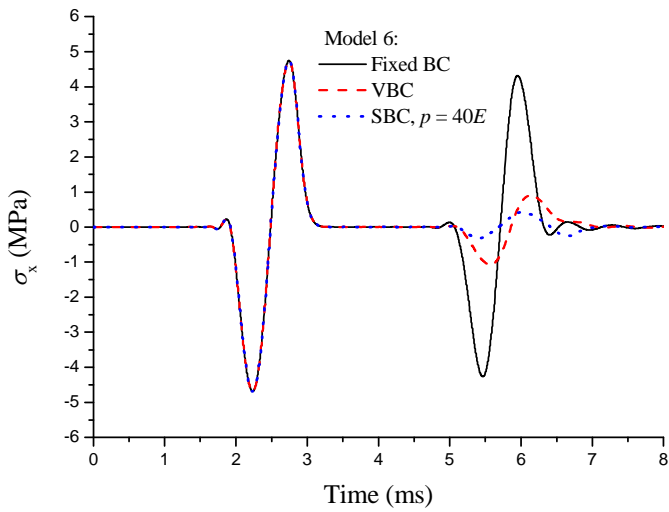
$$\mathbf{K}_{si} = p/\mathbf{T}_i^T \mathbf{F} \mathbf{T}_i \rightarrow \mathbf{K}_{ii} \tag{22}$$

where  $l$  is the length of the nonreflecting edge of a block and  $p$  is the newly applied constraint spring stiffness.

Fig. 11 shows horizontal stress time histories at the center of Model 5 and Model 6. The inclined boundaries at the right end of the models, which consist of block edges of various lengths, are set as the Fixed BC, the VBC, and the SBC, respectively. A complete period of sinusoidal seismic loading with a peak value of 5 MPa and a frequency of 1000 Hz is applied at the left ends of the bars to validate the absorbing abilities of the two nonreflecting boundary conditions to the compressive as well as



(a) incident angle = 30°



(b) incident angle = 60°

Figure 11: Absorbing ability under different stress wave incident angles at the boundary

the tensile stress waves. In these two models, the constraint spring stiffness  $p$  in the SBC is selected as  $70E$  and  $40E$ , respectively. It can be found that as compared with the reflected stress wave amplitudes obtained under the Fixed BC, the absorbing ability of the VBC to the reflections decreases with the increase of the incident angle of the seismic wave at the boundary; however, through the adjustment of the constraint spring stiffness, the reflections are absorbed satisfactorily by the SBC in both models.

## 4 A blasting-induced wave propagation problem in a jointed rock mass

### 4.1 Model descriptions

#### 4.1.1 Model geometry and numerical control parameters

The wave propagations in a small-scale underground blasting field test [Ma, Hao, and Zhou (1998)] is modeled by the DDA method to further verify this method in the prediction of wave propagations in real problems. In the test, an explosion chamber with the dimensions of  $8 \times 4 \times 2$  m was located at 115 m below the ground surface. The effective TNT charge weight is 606 kg with a loading density of  $10 \text{ kg/m}^3$ . This problem has been simplified as a two-dimensional UDEC model to investigate the propagations of the blasting-induced seismic waves [Fan, Jiao, and Zhao (2004)]. In the model, two sets of parallel joints with an even spacing of 2 m are generated to divide the surrounding rock media around the chamber into a jointed rock mass. The dip angles of the two joint sets are  $45^\circ$  and  $135^\circ$ , respectively. The same joint patterns are used to construct the DDA models. As shown in Fig. 12, the three DDA models have the dimensions of  $120 \times 120$  m,  $100 \times 100$  m, and  $80 \times 80$  m, respectively. The three different dimensions of the models are used to investigate the influence of the model size on the wave propagation modeling results. Two monitoring points (MPs) are placed in each model at the same locations. MP1 is 8 m right above the detonation center. MP2 is 6 m left and 5 m above the detonation center. In Model 2, the point right above the detonation center close to the boundary is also monitored (MP3).

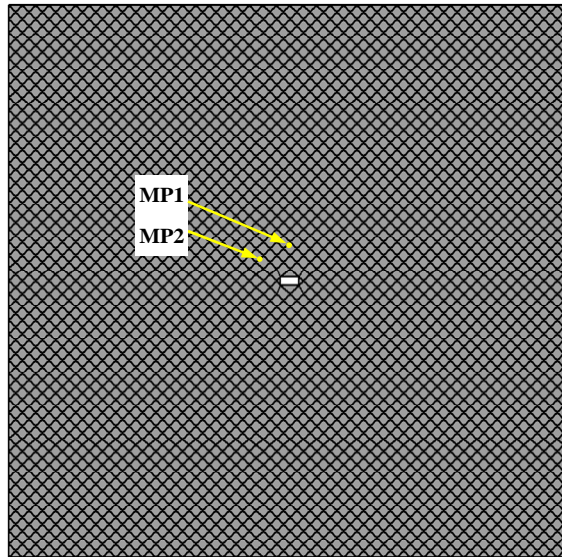
The rock blocks are assumed to be linear elastic with a density of  $\rho = 2650 \text{ kg/m}^3$ , a Young's modulus of  $E = 74 \text{ GPa}$ , and a Poisson's ratio of  $\mu = 0.2$ . The joints follow the Mohr-Coulomb failure criterion with a friction angle of  $\varphi = 25^\circ$ , a cohesion of  $c = 2.0 \text{ MPa}$ , and a zero tensile strength. All these parameters are the same as those used by Fan, Jiao, and Zhao (2004). The P-wave velocity of the intact rock can be derived as  $C_p = 5284.4 \text{ m/s}$ . The minimum height of the rock blocks is  $h_{\min} = 2 \text{ m}$ . The mass of the smallest block is  $m_{\min} = 1.06 \times 10^4 \text{ kg}$ . The normal stiffness of the joints is selected to be  $k_n = 100 \text{ GPa/m}$  in the UDEC model [Fan, Jiao, and Zhao (2004)]. According to Eq. (4), the normal contact spring

stiffness in the DDA model can be derived as  $g_0 = k_n l_0 / 2 = 100 \text{ GN/m}$ , where  $l_0 = 2 \text{ m}$  is the joint length between each pair of edge-to-edge contacted blocks. The maximum contact stiffness between blocks is  $K_{\max} = g_0$ . According to Eqs. (1) and (2), it can be derived that  $\Delta t^a = 3.78 \times 10^{-4} a$  and  $\Delta t^b = 6.51 \times 10^{-4} b$ , respectively. Based on these calculations, the upper limit of step time in the DDA modeling is chosen as  $g_1 = 10^{-5} \text{ s}$ , which implies that  $a$  is evaluated to be 0.026 and  $b$  is evaluated to be 0.015. The dynamic parameter and the maximum step displacement ratio are chosen as  $g_2 = 1$  and  $g_3 = 0.005$ , respectively. With these numerical control parameters, the step time does not change automatically in the open-close iterations throughout the DDA calculations, which indicates that these parameters are reasonably selected.

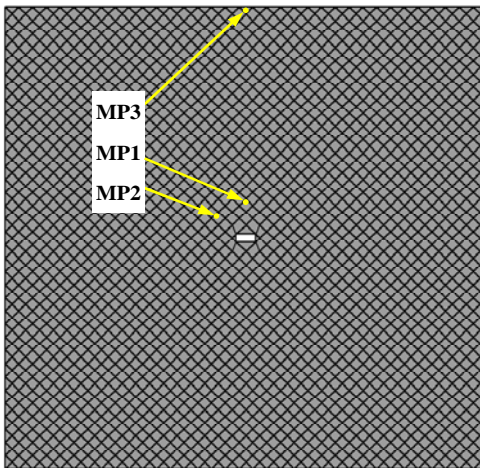
#### 4.1.2 Applications of blast loadings

The blast loading can be applied on the wall of the chamber in two forms. One is as prescribed force/stress and the other is as prescribed velocity/displacement. These two loading forms may yield the same results for homogeneous material, but different results for a jointed rock mass, as concluded by Fan, Jiao, and Zhao (2004). Our current DDA code enables the time-dependant loadings to be applied as force history input (FHI), stress/pressure history input (SHI), or displacement history input (DHI). The FHI and SHI will lead to the same results because these two approaches are equal essentially. In this paper, the applicability of the SHI approach and the DHI approach in the DDA to apply blast loadings to a jointed rock mass is to be investigated.

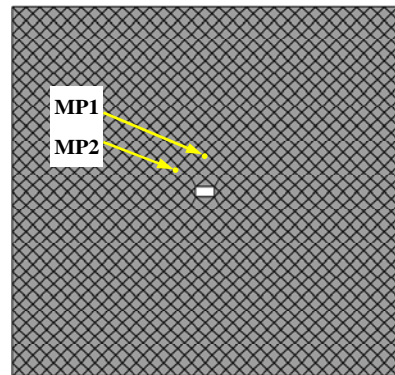
According to empirical equations in explosion dynamics, the blast loading on the chamber wall in the field test can be simplified as a triangular over-pressure time history [Fan, jiao, and Zhao (2004); Jiao, Zhang, Zhao, and Liu (2007)] with a maximum over-pressure of  $P_{\max} = 30.23 \text{ MPa}$ , a rise time of  $t_1 = 0.5 \text{ ms}$  and a total duration of  $t_2 = 2.5 \text{ ms}$ , as shown in Fig. 13a. The blast loading was also approximated to be a triangular particle velocity time history through DEM analysis on the same model without joints to be applied on the chamber wall of the jointed rock model by Fan, Jiao, and Zhao (2004). The rise time and the total duration of the velocity history are the same as those of the pressure history, and the peak value is 2.03 m/s. Similar approaches to estimate the blast loadings effected on a chamber wall have been widely employed [Chen and Zhao (1998); Lei, Hefny, Yan, and Teng (2007); Wang, Konietzky, and Shen (2009)]. When the record points are located in the surrounding rock mass close enough to the wall of the chamber, the blast loading obtained from a continuum-based numerical model can be identically applied in a discontinuum-based numerical model for a jointed rock mass [Chen and Zhao (1998)]. The particle velocity history is integrated to a displace-



(a) Model 1, 120m × 120m

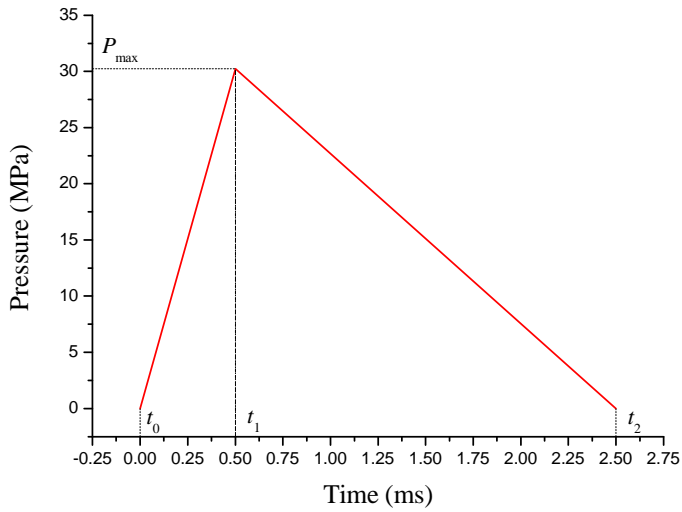


(b) Model 2, 100m × 100m

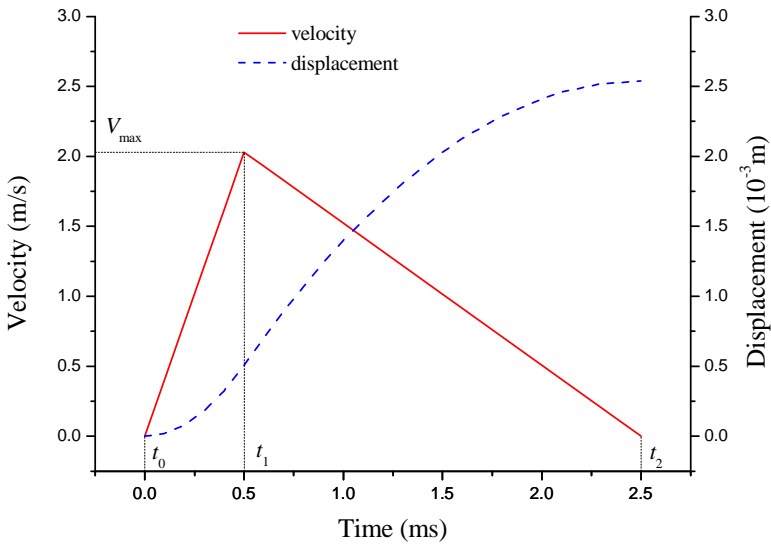


(c) Model 3, 80m × 80m

Figure 12: Three models for the blasting wave propagation simulation



(a) pressure time history for SHI



(b) velocity and displacement time histories for DHI

Figure 13: Two approaches for blast loading application

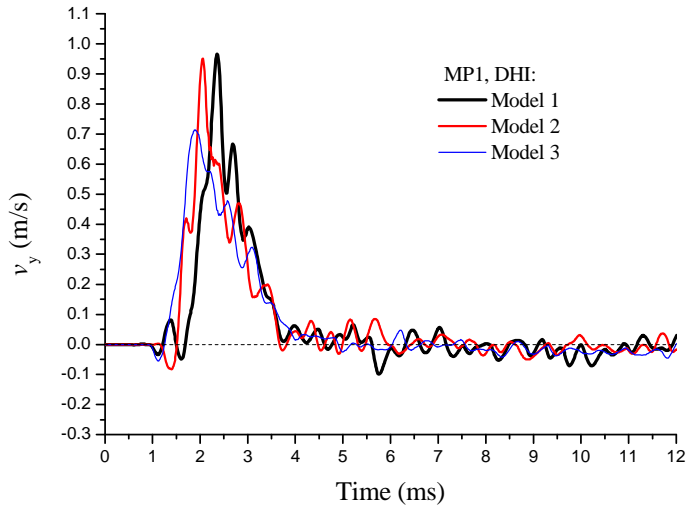
ment history to be applied in the DDA modeling. The velocity time history and the converted displacement time history are plotted in Fig. 13b. The applications of the displacement history and the velocity history will yield the same results because they are equivalent in essential to constrain the material particles to the same prescribed positions.

## 4.2 Modeling result analysis

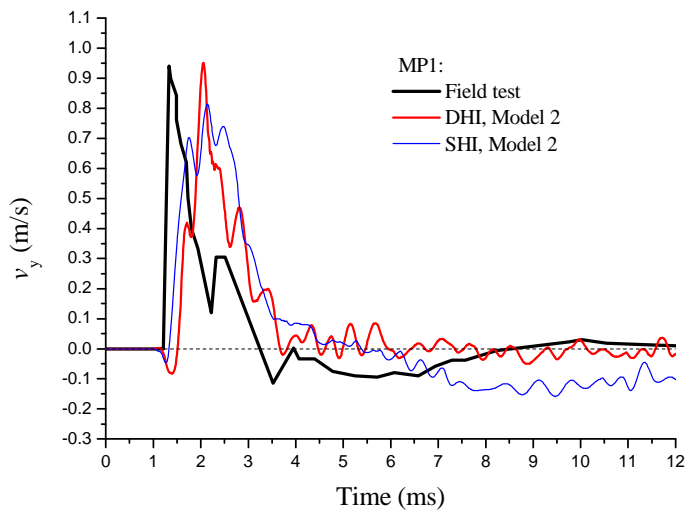
### 4.2.1 Influences of model size and loading approach

Fig. 14a gives the y-direction particle velocity time histories at MP1, where our interest focuses, in the early 12 ms in the three models. Within this period, the incident stress waves have not arrived at the outer boundaries. In the modeling, the blast loadings are applied on the chamber wall through the DHI approach and the outer boundaries of the models are totally fixed. The PPVs, acknowledged as the key factor controlling material damage, obtained in Model 1 and Model 2 are very close as 0.967 m/s and 0.951 m/s, respectively, while the PPV obtained in Model 3 is much smaller as 0.713 m/s. It indicates that the dimensions of Model 3 are too small for the problem because the incident stress waves in the near region around the chamber, where our interests focus, are distorted terribly. In fact, for a jointed rock mass with relatively low joint strength compared to the loading density, if the model size is too small, the movement of the rock blocks in the near region will certainly be disturbed by the restriction or release effect of the outer boundaries, no matter whatever boundary conditions are applied, thus the wave propagations in the near region are affected. The particle velocity time histories obtained in Model 2 and Model 1 differ slightly in detail. Such small differences are negligible in view of many uncertainties in a real rock mass problem. In terms of the derived particle velocity histories and the computational efficiency, Model 2 is regarded to have the reasonable dimensions for the problem, and this model will be used in the following simulations.

Fig. 14b is the y-direction particle velocity time history comparison at MP1 in the early 12 ms between the field test and the DDA results using the DHI and the SHI loading approaches. The outer boundaries of the model are set as the Fixed BC. The PPV obtained by the DHI approach in the DDA is 0.951 m/s, very close to the field test value of 0.95 m/s [Fan, Jiao, and Zhao (2004)]. The PPV obtained by the SHI approach in the DDA is 0.814 m/s, much smaller than the field result. In the UDEC modeling of the same problem [Fan, Jiao, and Zhao (2004)], the SHI approach derives a lower PPV as well, and the velocity history input approach/DHI approach also gets a PPV close to the field value. This is because the DHI approach is able to constrain the incident boundary to the prescribed position effectively and ensures good wave transmission through the joints near the boundary; on the



(a) velocity time histories at MP1 in three different models



(b) velocity time histories at MP1 with different loading methods

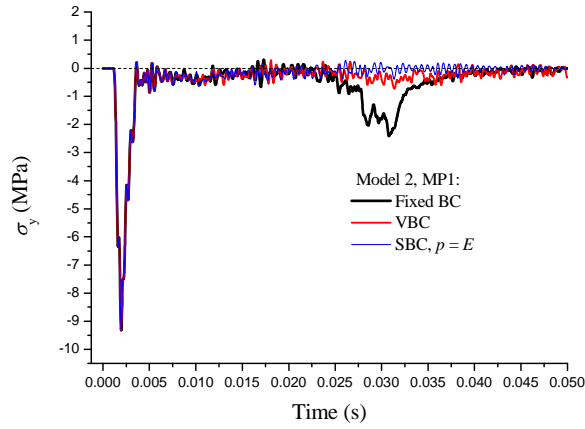
Figure 14: Influence of model size and blast loading application approach

contrary, the SHI approach cannot provide adequate displacement constraint to the boundary, which diminishes the transmissibility of the applied dynamic loading into the jointed rock mass. When the SHI approach is used, the reflections at the joints near the incident boundary will lead to the false opening of these joints and the subsequent backward movement of the boundary. In fact, in the field test, under the pressure of the expanding gas in the blasting chamber, the displacement history at the chamber wall should always be restricted in the early stage [Fan, Jiao, and Zhao (2004)]. As compared with the field test result, the particle velocity obtained by the DHI approach in the DDA rises to the peak value in a longer time. This phenomenon is also consistent with that obtained in the UDEC modeling [Fan, Jiao, and Zhao (2004)] as well as in another numerical modeling which employed an equivalent continuum model [Ma, Hao, and Zhou (1998)]. The lightly faster rise time of the field record could be attributed to the effect of a 0.2 m diameter instrumentation hole drilled through the chamber ceiling for placing the sensors [Ma, Hao, and Zhou (1998)]. Generally, it can be concluded that the DDA with the DHI loading approach derives satisfactory particle velocity time history at MP1 in this real problem.

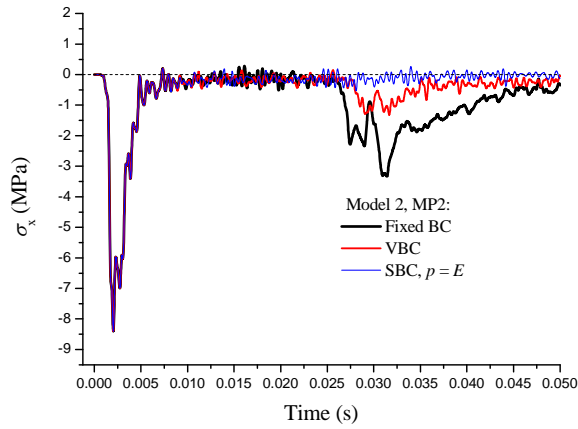
#### 4.2.2 Applications of nonreflecting boundary conditions

Here, the VBC and the SBC developed previously will be applied in the modeling of the field blasting problem. The outer boundaries of the DDA model are set as the Fixed BC, the VBC, and the SBC, respectively, and the DHI approach is used for the application of the blast loading. Through trial calculations, the constraint spring stiffness in the SBC is selected to be  $p = E$ , where  $E$  is the Young's modulus of the blocks. A relatively longer time, 0.05 s, of the wave propagations is calculated to investigate the reflecting effect of the boundaries to the waves.

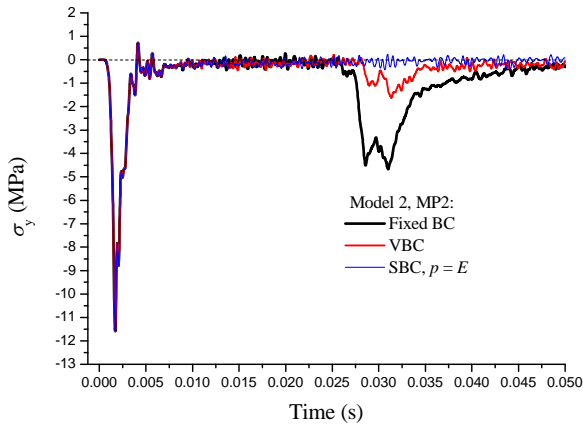
Fig. 15 gives the stress time histories in the  $y$  direction at MP1, and in the  $x$  and  $y$  directions at MP2. The corresponding particle velocity time histories are plotted in Fig. 16. Neglecting the reflections by the joints and the left and right outer boundaries, the wave propagations through MP1, which is located right above the chamber ceiling, could be approximately one-dimensional. The wave propagations through MP2 are much more complicated as a two-dimensional problem because the loadings applied on the ceiling and the left wall of the chamber will contribute the incident wave, and the left and upper outer boundaries will contribute the first reflected wave. Using the Fixed BC, obvious compressive stress waves are received at both of the two MPs after being reflected by the model outer boundaries, which lead to the later particle velocities back and forth after the incident PPVs. Such movements of the material particles will induce rock mass failures if the strength of the rock has been exceeded, and thus the modeling results will be distorted and



(a) MP 1, y direction

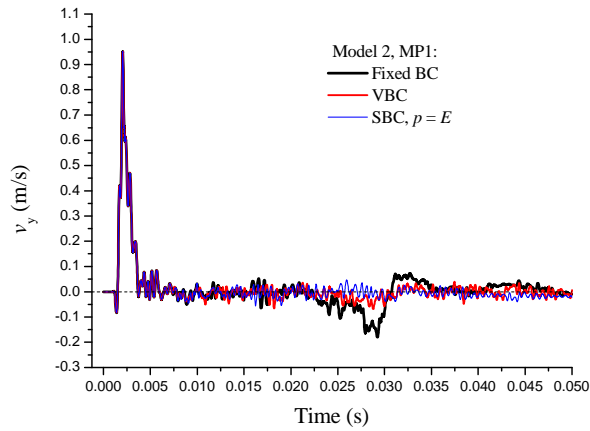


(b) MP 2, x direction

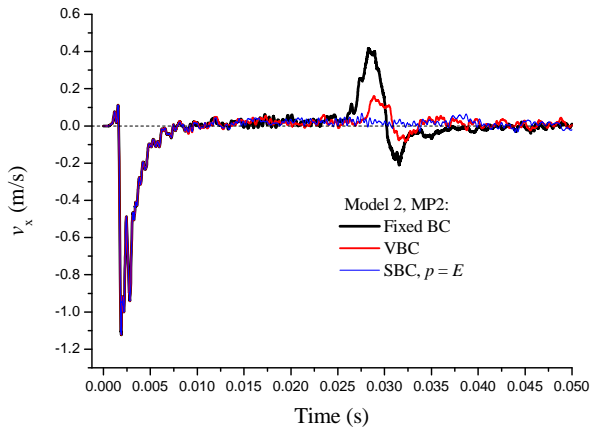


(c) MP 2, y direction

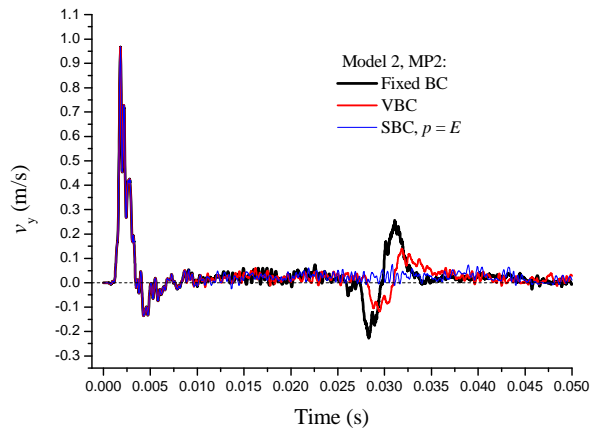
Figure 15: Stress time histories with different boundary conditions



(a) MP 1, y direction



(b) MP 2, x direction



(c) MP 2, y direction

Figure 16: Particle velocity time histories with different boundary conditions

become unreliable. Using the VBC, the reflections at MP1 are absorbed satisfactorily; however, the reflections at MP2 still exist with quite large amplitudes. Comparatively, the SBC almost totally eliminates all the reflections. These results indicate that, as compared with the VBC, the SBC is more applicable in absorbing reflections in such a complex two-dimensional wave propagation problem, where the stress waves may impinge the artificial boundaries from arbitrary angles.

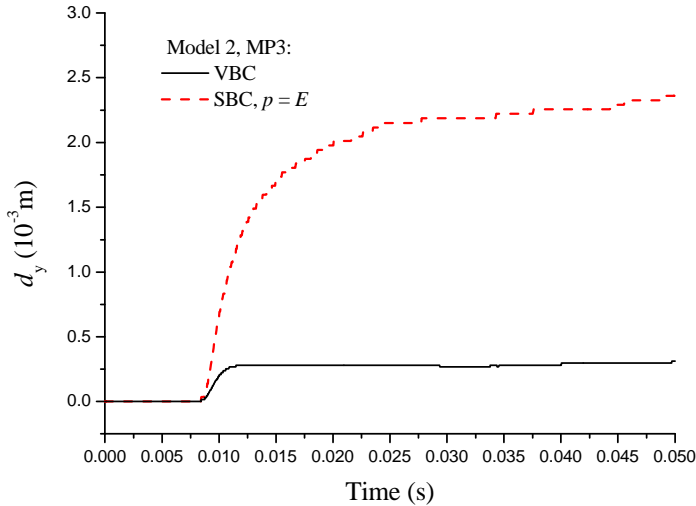


Figure 17: Displacement time history at boundary

As indicated in Section 3, using the SBC with relatively small constraint spring stiffness, a boundary shift problem may appear. The displacement time histories in the  $y$  direction at MP3 in the DDA modeling are plotted in Fig. 17. It can be found that, as compared with the VBC, the SBC with constraint spring stiffness of  $p = E$  leads to larger particle motions at the boundary. The final displacement under the SBC is  $2.36 \times 10^{-3}$  m. As compared with the model size, such a small displacement at the outer boundary could produce negligible influences on the block motions in the near region around the blasting chamber.

Fig. 18 gives the comparison of the PPV attenuation in the rock mass right above the blasting chamber between the field records and the DDA results using the SBC with  $p = E$  for the outer boundaries. The empirical line is obtained by fitting the field test records into the following equation [Ma, Hao, and Zhou (1998)]:

$$PPV = 1.8 \left( \frac{R}{Q^{1/3}} \right)^{-2.5} \quad (\text{m/s}) \quad (23)$$

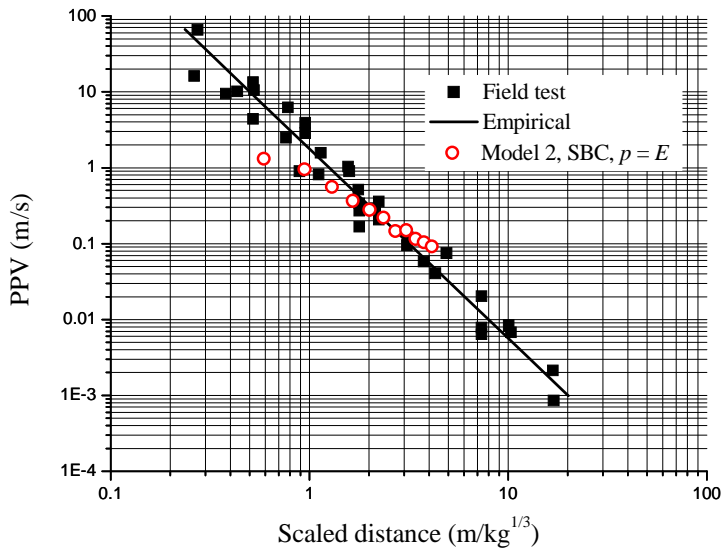


Figure 18: PPV attenuation comparison between DDA results and filed test

where  $R$  is the distance from the charge center towards the upper outer boundary measured in meters;  $Q$  is the charge weight measured in kg;  $R/Q^{1/3}$  is called the scaled distance. In the figure, it can be found that the numerically derived points by the DDA method fall in the range of the field records and distribute in a near range at the two sides of the empirical line quite satisfactorily. The DDA derived points lie below the empirical line in the near region of the blasting chamber and above the empirical line in the relatively far region. This varying trend is similar to that reported by Ma, Hao, and Zhou (1998) and Fan, Jiao, and Zhao (2004). The divergences between the numerical results and the field test could be attributed to the discrepancies between a numerical model and the real problem; given that there are so many uncertainties in the field test, the DDA predicted PPV attenuation result is regarded to be favorably acceptable. This result also further indicates that the SBC works well as a nonreflecting boundary in such complex two-dimensional wave propagation problems.

## 5 Discussions and conclusions

The DDA, as a typical discontinuum-based numerical method, is especially suitable for modeling the mechanical behaviors of jointed rock masses. For the modeling of wave propagations in a jointed rock mass, the upper limit of step time should be chosen carefully combining a reasonable evaluation of the maximum step dis-

placement ratio to fulfill the infinitesimal deformation/displacement assumption in one time step. A way for the selection of the numerical control parameters is presented and verified in this paper. The maximum step displacement ratio is chosen according to Shi's DDA user's manual. The upper limit of step time is decided based on a group of formulas. In the DDA calculation, if the given step time does not change in the open-close iterations, the selected step time can be regarded small enough. In addition, without further internal discretization, the first-order DDA is only applicable for modeling wave propagations in a relatively heavily jointed rock mass because the block ratio requirement, recommend as smaller than 1/16, must be satisfied.

The DDA takes the penalty contact method to describe the block interface behaviors, thus the joints modeled are of linear elastic properties. In this paper, by assuming that the two half spaces of a joint in the DDA just have parallel movements, the joint stiffness is approximated from the contact spring stiffness that is used in the penalty method. With the increase of the contact stiffness/joint stiffness, the amplitude of the stress wave propagating in a jointed rock mass attenuates slower with a smaller time delay. The increase of the seismic loading frequency helps to accelerate the amplitude attenuation, but has little influence on the wave velocity. When the joint strength is relatively low compared to the loading intensity, the opening and/or slip of the joint interfaces may affect the wave propagations remarkably, and the influence also depends on the wave incident angle to the joint. With a relatively low joint strength, the increase of the incident angle leads to a faster amplitude attenuation and a larger wave velocity. These conclusions drawn from the DDA modeling examples of wave propagations in jointed rock bars are consistent with those recognitions in available literatures. The blast loading time histories are applied via the DHI approach and the SHI approach in the DDA. The DHI approach constrains the incident boundary to the prescribed position effectively and thus derives more reliable modeling results of blasting-induced wave propagations in a jointed rock mass. As compared with the field test results, the DDA predicts the wave propagations in a two-dimensional jointed rock problem quite well.

Regarding the two nonreflecting boundary conditions, the absorbing ability of the VBC is affected by the boundary block edge length and the stress wave incident angle at the boundary. The VBC is more applicable in simple problems with small incident angles. The absorbing ability of the SBC can be increased to a very satisfactory level even in very complex wave propagation problems by optimizing the constraint spring stiffness through trial calculations. The trial calculation method is feasible on many occasions although it costs the computer run-time. For a real problem, e.g, rock blasting, the time required for the stress waves to reach the artificial boundaries is much less than that required for the material to be damaged or

even displaced. To avoid the possible boundary shift problem induced by the SBC with relatively low constraint spring stiffness, the calculation domain should be enlarged to a certain extent. In fact, for a dynamic problem in an infinite jointed rock mass with relatively low joint strength, the model size cannot be too small no matter whatever boundary condition is applied, as revealed in the modeling example of the field blasting problem in Section 4.

The current DDA is only applicable for modeling wave propagations in a relatively heavily jointed rock mass with linear elastic joints. Block internal discretization can make this method applicable for modeling wave propagations in a rock mass with arbitrary joint distributions. For a more realistic modeling of the wave propagations in real problems, nonlinear and viscous properties of the block interfaces should be considered in the DDA.

**Acknowledgement:** This research is supported by the Underground Technology and Rock Engineering (UTRE) Phase II, Singapore, the National Natural Science Foundation of China No. 51204137, and the Research Foundation of Southwest University of Science and Technology No. 12zx7104.

## References

- Bao H. R.; Hatzor Y. H.; Huang X.** (2012): A new viscous boundary condition in the two-dimensional discontinuous deformation analysis method for wave propagation problems. *Rock Mechanics and Rock Engineering*, vol. 45, no. 5, pp. 919–928.
- Cai J. G.; Zhao J.** (2000): Effects of multiple parallel fractures on apparent attenuation of stress waves in rock masses. *International Journal of Rock Mechanics and Mining Sciences*, vol. 37, no. 4, pp. 661-682.
- Cai Y. G.; He T.; Wang R.** (2000): Numerical simulation of dynamic process of the Tangshan earthquake by a new method - LDDA. *Pure and Applied Geophysics*, vol. 157, no. 11-12, pp. 2083-2104.
- Chen S. G.** (1999): *Discrete Element Modeling of Jointed Rock Masses under Dynamic Loading*. Dissertation, Nanyang Technological University.
- Chen S. G.; Zhao J.** (1998): A study of UDEC modelling for blast wave propagation in jointed rock masses. *International Journal of Rock Mechanics and Mining Sciences*, vol. 35, no. 1, pp. 93-99.
- Cook N. G. W.** (1992): Natural joints in rock - mechanical, hydraulic and seismic behavior and properties under normal stress. *International Journal of Rock Mechanics and Mining Sciences*, vol. 29, no. 3, pp. 198-223.

- Cundall P. A.** (1971): A computer model for simulating progressive, large-scale movements in blocky rock systems. In: *Proceedings of the International Symposium on Rock Mechanics*, Nancy, France, pp. 11-18.
- Fan S. C.; Jiao Y. Y.; Zhao J.** (2004): On modelling of incident boundary for wave propagation in jointed rock masses using discrete element method. *Computers and Geotechnics*, vol. 31, no. 1, pp. 57-66.
- Gu B. L.; Suarez-Rivera R.; Nihei K. T.; Myer L. R.** (1996): Incidence of plane waves upon a fracture. *Journal of Geophysical Research-Solid Earth*, vol. 101, no. B11, pp. 25337-25346.
- Gu J.; Zhao Z. Y.** (2009): Considerations of the discontinuous deformation analysis on wave propagation problems. *International Journal for Numerical and Analytical Methods in Geomechanics*, vol. 33, no. 12, pp. 1449-1465.
- Hatzor Y. H.; Arzi A. A.; Zaslavsky Y.; Shapira A.** (2004): Dynamic stability analysis of jointed rock slopes using the DDA method: King Herod's Palace, Masada, Israel. *International Journal of Rock Mechanics and Mining Sciences*, vol. 41, no. 5, pp. 813-832.
- Hatzor Y. H.; Feintuch A.** (2001): The validity of dynamic block displacement prediction using DDA. *International Journal of Rock Mechanics and Mining Sciences*, vol. 38, no. 4, pp. 599-606.
- Jiao Y. Y.; Zhang X. L.; Zhao J.; Liu Q. S.** (2007): Viscous boundary of DDA for modeling stress wave propagation in jointed rock. *International Journal of Rock Mechanics and Mining Sciences*, vol. 44, no. 7, pp. 1070-1076.
- Kamai R.; Hatzor Y. H.** (2008): Numerical analysis of block stone displacements in ancient masonry structures: A new method to estimate historic ground motions. *International Journal for Numerical and Analytical Methods in Geomechanics*, vol. 32, no. 11, pp. 1321-1340.
- Kong X. J.; Liu J.** (2002): Dynamic failure numeric simulations of model concrete-faced rock-fill dam. *Soil Dynamics and Earthquake Engineering*, vol. 22, no. 9-12, pp. 1131-1134.
- Kuhlmeyer R. L.; Lysmer J.** (1973): Finite element method accuracy for wave propagation problems. *Journal of Soil Mechanics and Foundation Division, ASCE*, vol. 99, pp. 421-427.
- Last N. C.; Harper T. R.** (1990): Response of fractured rock subject to fluid injection. 1. development of a numerical-model. *Tectonophysics*, vol. 172, no. 1-2, pp. 1-31.
- Lei W. D.; Hefny A. M.; Yan S.; Teng J.** (2007): A numerical study on 2-D compressive wave propagation in rock masses with a set of joints along the radial

direction normal to the joints. *Computers and Geotechnics*, vol. 34, no. 6, pp. 508-523.

**Li J. C.; Ma G. W.; Huang X.** (2010): Analysis of wave propagation through a filled rock joint. *Rock Mechanics and Rock Engineering*, vol. 43, no. 6, pp. 789-798.

**Li J. C.; Ma G.; Zhao J.** (2010): An equivalent viscoelastic model for rock mass with parallel joints. *Journal of Geophysical Research-Solid Earth*, vol. 115, B03305, doi:10.1029/2008JB006241.

**Li J. C.; Ma G. W.; Zhao J.** (2011a): Analysis of stochastic seismic wave interaction with a slippery rock fault. *Rock Mechanics and Rock Engineering*, vol. 44, no. 1, pp.85-92.

**Li J. C.; Ma G. W.; Zhao J.** (2011b): Stress wave interaction with a nonlinear and slippery rock joint. *International Journal of Rock Mechanics and Mining Sciences*, vol. 48, no. 3, pp. 493-500.

**Lin Y. H.; Ma C. C.** (2011): Transient analysis of elastic wave propagation in multilayered structures. *CMC-Computers, Materials & Continua*, vol. 24, no. 1, pp. 15-42.

**Liu L. Q.; Katsabanis P. D.** (1997): Development of a continuum damage model for blasting analysis. *International Journal of Rock Mechanics and Mining Sciences*, vol. 34, no. 2, pp. 217-231.

**Lysmer J.; Kuhlemeyer R. L.** (1969): Finite dynamic model for infinite media. *Journal of the Engineering Mechanics Division, ASCE*, vol. 95, no. EM4, pp. 859-877.

**Ma G. W.; Hao H.; Zhou Y. X.** (1998): Modeling of wave propagation induced by underground explosion. *Computers and Geotechnics*, vol. 22, no. 3-4, pp. 283-303.

**Ma G. W.; Li J. C.; Zhao J.** (2011): Three-phase medium model for filled rock joint and interaction with stress waves. *International Journal for Numerical and Analytical Methods in Geomechanics*, vol. 35, no. 1, pp. 97-110.

**MacLaughlin M. M.; Doolin D. M.** (2006): Review of validation of the discontinuous deformation analysis (DDA) method. *International Journal for Numerical and Analytical Methods in Geomechanics*, vol. 30, no. 4, pp. 271-305.

**Mortazavi A.; Katsabanis P. D.** (2001): Modelling burden size and strata dip effects on the surface blasting process. *International Journal of Rock Mechanics and Mining Sciences*, vol. 38, no. 4, pp. 481-498.

**Ning Y. J.** (2008): *Study on Dynamic and Failure Problems in DDA Method and Its Application*. Dissertation, Beijing Institute of Technology.

- Ning Y. J.; Yang J.; An X. M.; Ma G. W.** (2011): Modelling rock fracturing and blast-induced rock mass failure via advanced discretisation within the discontinuous deformation analysis framework. *Computers and Geotechnics*, vol. 38, no. 1, pp. 40-49.
- Ning Y. J.; Yang J.; Ma G. W.; Chen P. W.** (2009): DDA for dynamic failure problems and its application in rock blasting simulation. In: *Proceeding of the 9th International Conference on Analysis of Discontinuous Deformation (ICADD9)*. Singapore, pp. 83-90.
- Ning Y. J.; Yang J.; Ma G. W.; Chen P. W.** (2011): Modelling rock blasting considering explosion gas penetration using discontinuous deformation analysis. *Rock Mechanics and Rock Engineering*, vol. 44, no. 4, pp. 483-490.
- Ning Y. J.; Zhao Z. Y.** (2012): A detailed investigation of block dynamic sliding by the discontinuous deformation analysis. *International Journal for Numerical and Analytical Methods in Geomechanics*, DOI:10.1002/nag.2140.
- Pyrak-Nolte L. J.; Myer L. R.; Cook N. G. W.** (1990a): Transmission of seismic-waves across single natural fractures. *Journal of Geophysical Research-Solid Earth and Planets*, vol. 95, no. B6, pp. 8617-8638.
- Pyrak-Nolte L. J.; Myer L. R.; Cook N. G. W.** (1990b): Anisotropy in seismic velocities and amplitudes from multiple parallel fractures. *Journal of Geophysical Research-Solid Earth and Planets*, vol. 95, no. B7, pp. 11345-11358.
- Qian Y.** (2008): *Simulation Study on Dynamics, Damage and Fracture of Brittle Material by Numerical Manifold Method*. Dissertation, Beijing Institute of Technology.
- Resende R.; Lamas L. N.; Lemos J. V.; Calcada R.** (2010): Micromechanical modelling of stress waves in rock and rock fractures. *Rock Mechanics and Rock Engineering*, vol. 43, no. 6, pp. 741-761.
- Schoenberg M.; Muir F.** (1989): A calculus for finely layered anisotropic media. *Geophysics*, vol. 54, no. 5, pp. 581-589.
- Schoenberg M.; Sayers C. M.** (1995): Seismic anisotropy of fractured rock. *Geophysics*, vol. 60, no. 1, pp. 204-211.
- Shi G. H.** (1988): *Discontinuous Deformation Analysis: A new Numerical Model for the Statics and Dynamics of Block Systems*. Dissertation, UC Berkeley.
- Smith W. D.** (1974): Nonreflecting plane boundary for wave-propagation problems. *Journal of Computational Physics*, vol. 15, no. 4, pp. 492-503.
- Tserpes K. I.; Koumpias A. S.** (2012): Comparison between a cohesive zone model and a continuum damage model in predicting mode-I fracture behavior of adhesively bonded joints. *CMES-Computer Modeling in Engineering & Sciences*,

vol. 83, no. 2, pp. 169-181.

**Wang Z. J.** (2001): Fundamentals of seismic rock physics. *Geophysics*, vol. 66, no. 2, pp. 398-412.

**Wang Z. L.; Konietzky H.; Shen R. F.** (2009): Coupled finite element and discrete element method for underground blast in faulted rock masses. *Soil Dynamics and Earthquake Engineering*, vol. 29, no. 6, pp. 939-945.

**Wu J. H.** (2010): Seismic landslide simulations in discontinuous deformation analysis. *Computers and Geotechnics*, vol. 37, no. 5, pp. 594-601.

**Wu J. H.; Lin J. S.; Chen C. S.** (2009): Dynamic discrete analysis of an earthquake-induced large-scale landslide. *International Journal of Rock Mechanics and Mining Sciences*, vol. 46, no. 2, pp. 397-407.

**Yagoda-Biran G.; Hatzor Y. H.** (2010): Constraining paleo PGA values by numerical analysis of overturned columns. *Earthquake Engineering & Structural Dynamics*, vol. 39, no. 4, pp. 463-472.

**Zhang X. P.; Wong L. N. Y.; Wang S. J.; Han G. Y.** (2011): Engineering properties of quartz mica schist. *Engineering Geology*, vol. 121, no. 3-4, pp. 135-149.

**Zhao J.; Cai J. G.** (2001): Transmission of elastic P-waves across single fractures with a nonlinear normal deformational behavior. *Rock Mechanics and Rock Engineering*, vol. 34, no. 1, pp. 3-22.

**Zhao J.; Zhao X. B.; Cai J. G.** (2006): A further study of P-wave attenuation across parallel fractures with linear deformational behaviour. *International Journal of Rock Mechanics and Mining Sciences*, vol. 43, no. 5, pp. 776-788.